Journal of Computational and Nonlinear Dynamics. December 11, 2024;
Accepted manuscript posted April 11, 2025. 10.1115/1.4068426

Nonlinear Model Predictive Control of Urban Air Mobility Aircraft with Gust Disturbance

Jessica S. M. Nunes
Ph.D., ASME Student Member
Depart. of Aerospace Eng. and Mechanics
The University of Alabama
Tuscaloosa, Alabama 35487-0280
Email: jsnunes@crimson.ua.edu

Weihua Su*
Associate Professor, Member of ASME
Depart. of Aerospace Eng. and Mechanics
The University of Alabama
Tuscaloosa, Alabama 35487-0280
Email: suw@eng.ua.edu

Tianyi He
Assistant Professor, Member of ASME
Depart. of Mechanical and Aerospace Eng.
Utah State University
Logan, Utah 84322
Email: tianyi.he@usu.edu

The paper explores improving the ride quality of urban air mobility (UAM) aircraft by using a nonlinear model predictive controller (NMPC) for trajectory tracking in the presence of gusts. A hybrid UAM aircraft with traditional control surfaces and multiple rotors is studied. The aircraft's free-flight behavior is governed by a set of nonlinear rigid-body dynamic equations that consider the gyroscopic and inertial effects of the tiltrotors. The control inputs for the aircraft include the spin rate and acceleration of the rotors, their tilt angle and rate, and the deflections of traditional control surfaces, such as the elevator, aileron, and rudder. This research numerically studies the effects of NMPC in actively suppressing aircraft's dynamic responses to continuous stochastic gusts or discrete "1-cosine" gusts, which are applied symmetrically and asymmetrically on the lifting surfaces. The findings indicate that NMPC can effectively maintain the aircraft on its desired flight path, closely resembling the undisturbed level flight when it experiences moderate-intensity gusts. However, the controller's effectiveness decreases as the intensity of the gusts increases. The NMPC can no longer constrain the flight path deviation within a bounded range due to an increased pitch rate when the gust intensity surpasses a certain threshold. In addition, the discrete "1-cosine" gusts present more significant challenges, resulting in pitch angle deviations from the desired value, even at low gust magnitudes.

NOMENCLATURE

G	Global coordinate frame
B	Body coordinate frame
$\mathbf{p}_{G/B}$	Aircraft mass center in O_B, m
$\mathbf{v}_B$	Translational velocity vector, $\mathrm{m\,s^{-1}}$
$\boldsymbol{\omega}_B$	Angular velocity vector, $\mathrm{rad\,s^{-1}}$
$\boldsymbol{\theta}_B$	Rigid-body rotation angles, rad
$\mathbf{M}_{BB}$	Inertia matrix
$\mathbf{C}_{BB}$	Damping matrix
$\mathbf{R}_B$	Aircraft load vector
$\mathbf{R}^{\text{grav}}$	Gravity load
$\mathbf{R}^{\text{iner}}$	Inertial loads
$\mathbf{R}^{\text{rate}}$	Induced moment due to tiltrotors
$\mathbf{R}^{\text{gyro}}$	Gyroscopic loads
$\mathbf{R}^{\text{ext}}$	External loads
$\boldsymbol{\Omega}_\zeta$	Rigid-body angular velocities function
$\mathbf{C}^{GB}$	Rotational matrix - body to global
$\mathbf{x}$	System states
$\mathbf{u}$	System control inputs
$\mathbf{y}$	System outputs
$\boldsymbol{\Phi}$	Euler angle vector

*Corresponding author

ϕ Roll angle, deg
θ Pitch angle, deg
ψ Yaw angle, deg
m_B Body mass, kg
I_B Body moment of inertia, $\mathrm{kg\,m^2}$
m_r Rotor mass, kg
I_r^e Rotor moment of inertia, $\mathrm{kg\,m^2}$
$\boldsymbol{\beta}$ Rigid-body velocity vector
$\boldsymbol{\zeta}$ Quaternions vector
$\mathbf{p}_B^G$ Inertial position vector of O_B, m
$\delta_e, \delta_a, \delta_r$ Elevator, aileron and rudder angles, deg
$\boldsymbol{\Xi}$ Rotor tilt angle, deg
$\boldsymbol{\Gamma}$ Rotor spin angle, deg
J Cost function
p Prediction horizon
n Control horizon
$\mathbf{U}_k$ Quadratic problem decision vector
$\mathbf{r}$ Output reference vector
w^i Variable i NMPC weight
s^i Variable i NMPC scale factor
$u_{j,\text{target}}$ Target of the j^{th} input
$\mathbf{u}_{\text{min/max}}$ Input limits vector
$\Delta\mathbf{u}_{\text{min/max}}$ Input rate limits vector
V_{w}, V_t Gust vertical velocity at the wing and tail
$\Phi_{\text{w}}(\omega)$ Gust with velocity spectra
σ_{w} Vertical turbulence intensity
L_{w} Turbulence scale length
V Aircraft flight speed through a frozen turbulence field
ω Turbulent gust frequency
$\Delta\omega$ Turbulent gust frequency step
Ψ Random gust phase shift in rad
Δy_{tail} Northwise distance between tail and wing nodes
$p_{B,y0}^G$ y-coord. at which aircraft enters discrete gust
H Discrete gust gradient
V_{max} Discrete gust velocity

1 INTRODUCTION

The Urban Air Mobility (UAM) market is projected to experience significant growth, expanding from $ 7.1 billion in 2021 to $ 90 billion by 2050. This growth is driven by UAM's potential to revolutionize transportation [1]. UAM applications are expected to be diverse, encompassing personal commuting, on-demand air taxis with passenger-defined routes, air metro systems with fixed public transport routes, airport and company shuttles, regional public transport, air ambulances, package delivery, law enforcement, and military operations [2, 3]. These applications will have a considerable impact on services provided by both public and private institutions across various sectors. As the development progresses, enhancing flight safety, automation, and ride quality is more crucial than ever to integrate these new aircraft safely into urban airspace [4, 5, 6].

A key segment of UAM is the distributed electric propulsion (DEP) enabled vertical takeoff and landing (VTOL) vehicles, commonly known as eVTOLs [7]. These vehicles employ a fixed-wing design with multiple tiltrotors to enable vertical takeoff and landing. The tilt and spin of the rotors also function as actuators, enhancing safety through redundancy, i.e., with multiple rotors, these vehicles can continue operating even in case of motor or rotor failure, thereby reducing the risk of serious incidents. eVTOLs also hold significant potential for autonomous and semi-autonomous flight, which could reduce accidents caused by human error, which is a significant factor in aviation incidents, and improve navigation in complex urban environments by enabling aircraft to avoid obstacles and adapt to dynamic conditions [8, 9].

Ride quality is essential for urban passenger transportation, one of the significant functions of UAM aircraft. Improving ride quality involves tackling several challenges, such as noise reduction, which remains difficult to achieve at levels suitable for cities. Several studies have focused on quieter rotor designs and optimized flight paths to lessen noise pollution [10, 11].

Aircraft response to external air disturbances, e.g., gust, and the control of vibration and trajectory of such aircraft is also critical for passenger comfort and aircraft performance and safety [12]. The development of autonomous flight systems adds to the complexity of ride quality, demanding robust algorithms to manage turbulence efficiently. In their comprehensive review, Kim et al. [13] noted that early quadrotor control developments relied on linear controllers like Linear Quadratic Regulator (LQR) and Proportional–Integral–Derivative (PID) controllers. These controllers were effective for maintaining stability during level flight and hovering. However, they exhibited limitations in more challenging conditions, such as high-speed flights and environments with wind disturbances, as observed by Hoffmann et al. [14] in flight tests using a PID controller. Zhang et al. [15] investigated the flight stabilization and gust control of the XV-15 tiltrotor aircraft using an optimal control method based on quadratic programming. Their approach employed a Linear Time-Varying (LTV) model to accurately capture the aircraft's dynamic characteristics through online linearization of the nonlinear model to update the model parameters at each sampling constant. The controller is designed based on the LTV model and incorporated with the input constraints. The results indicated that the controller successfully achieved the desired tracking perfor-

mance throughout the operational envelope, including the transition flights, and the ability to attenuate gust disturbance.

Alternatively, Model Predictive Control (MPC) is a robust approach for controlling dynamic systems [16, 17]. It has the potential for aircraft control, especially when the aircraft is subject to external disturbance. It utilizes a dynamic model to predict future responses and determine optimal inputs for achieving target trajectories [18, 19]. Qin and Badgwell [20] conducted a comprehensive examination of the history and industrial applications of MPC algorithms. Notable reviews of MPC theory can also be found in several publications [21, 22, 23] as well as books [24, 25, 26]. He and Su [27] explored the use of MPC based on linear parameter-varying (LPV) models to suppress vibrations and alleviate gust loads for highly flexible aircraft. The dynamic equation was firstly linearized around a series of equilibria and model reduction was performed for each linearized model. A scheduling parameter was then chosen to parameterize and interpolate the linearized models to render a reduced-order LPV model. This work's main innovation was using the magnitude of the first symmetric bending mode as the LPV scheduling parameter, compared to using the gust-induced angle of attack at the wing root. Both parameter selections were evaluated for gust alleviation when the flexible aircraft faced a uniformly applied gust perturbation across the entire wing. The control input was the conventional trailing-edge flaps on the main wings and tails. The simulation results demonstrated that the controller designed using the modal magnitude as LPV parameter performed better in suppressing gusts when compared to using the gust-induced angle of attack.

Moreover, Nonlinear Model Predictive Control (NMPC) has gained considerable attention in the aerospace research community, while the computational burden associated with this method usually limits its application. The work by Meradi et al. [28] investigated the stochastic gust control of a quadrotor VTOL with NMPC, sliding mode control (SMC), and integral backstepping control (IBC). While the NMPC was shown to have a higher computational cost than SMC and IBC, it showed minimum control effort. They proposed a new controller, predictive sliding mode control (PSMC), combining SMC and NMPC. A recent study investigated NMPC's effectiveness for vibration suppression and lateral path tracking in a fixed-wing six-tiltrotor eVTOL [29]. In this study, the NMPC performance was compared to open-loop, LQR, and linear MPC. Results showed that both NMPC and LQR effectively suppressed vibrations, whereas the linear MPC was ineffective in mitigating rigid-body oscillations. For path tracking, NMPC outperformed LQR because the LQR control performance was limited by the linearized model of the tiltrotor dynamics. In contrast, NMPC's capacity to predict future aircraft states and account for system nonlinearity led to better path tracking. The authors expanded the study on UAM aircraft flight safety by evaluating the NMPC for flight control under control effectors failure [30]. The results indicate that the NMPC can effectively attenuate the perturbation caused by an asymmetric tiltrotor failure by utilizing the back rotors as push thrusters. Moreover, when employing the back rotors for pitch control, the NMPC significantly reduces the phugoid mode vibrations caused by the elevator failure.

The dynamic behavior of tiltrotor aircraft is inherently highly nonlinear, where NMPC is a promising technique for analyzing the control of such aircraft, especially when subjected to gust excitation. Thanks to the Lidar/radar sensors, the gust ahead of the aircraft can be measured. Therefore, NMPC can incorporate the gust measurements into predicting the nonlinear system responses, and find finite-horizon optimal control inputs to attenuate the gust. The NMPC accounts for the full nonlinear dynamic model, which is more accurate than linearized or LPV models in capturing transient dynamics between equilibrium conditions. Therefore, this paper investigates the effects of NMPC for active gust attenuation of continuous stochastic and discrete gusts, which are applied symmetrically and asymmetrically on lifting surfaces of a tiltrotor aircraft. This paper is organized as follows. Section 2 introduces the nonlinear flight dynamic formulation for tiltrotor aircraft, followed by the control systems description in Section 3. Section 4 shows the numerical results. Finally, conclusions are summarized in Section 5.

2 FLIGHT DYNAMIC FORMULATIONS

This study investigates a hybrid urban air mobility (UAM) aircraft that consists of a fixed-wing airplane with tiltrotors (see Fig. 1). This section presents a condensed summary of these equations. One can refer to [31] for more details on the formulation.

A body-fixed frame B is defined with respect to the inertial frame G, with B_x pointing to the right wing, B_y pointing forward, and B_z completing the right-hand rule. While the B frame can be arbitrarily placed, it is convenient to set the frame's origin O_B within the vehicle's symmetric plane. The inertial position of O_B is represented by $\mathbf{p}_B$, while $\mathbf{p}_{G/B}$ describes the position of the mass center of the fixed-wing aircraft (excluding the tiltrotors) with respect to the B frame. The aircraft's

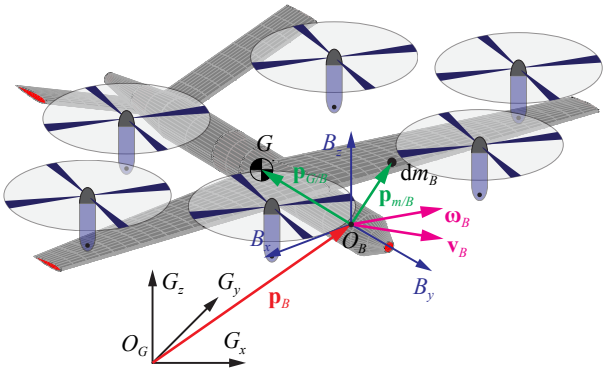

Fig. 1: Global and body reference frames of a rigid-body tiltrotor aircraft (connections between rotors and aircraft are not shown)

rigid-body velocity is given by

$$\boldsymbol{\beta} = \begin{Bmatrix} \mathbf{v}_B \\ \boldsymbol{\omega}_B \end{Bmatrix} = \begin{Bmatrix} \dot{\mathbf{p}}_B + \boldsymbol{\omega}_B \times \mathbf{p}_B \\ \dot{\boldsymbol{\theta}}_B \end{Bmatrix} \tag{1}$$

By following the Hamilton's principle, the governing equation of motion is obtained, given by

$$\mathbf{M}_{BB}(\boldsymbol{\Xi})\dot{\boldsymbol{\beta}} + \mathbf{C}_{BB}(\boldsymbol{\beta}, \boldsymbol{\Xi})\boldsymbol{\beta} = \mathbf{R}_B \tag{2}$$

where the inertia matrix $\mathbf{M}_{BB}$ is dependent on the tilt angles $\boldsymbol{\Xi}$ of the rotors, while the damping matrix $\mathbf{C}_{BB}$ is dependent on both $\boldsymbol{\beta}$ and $\boldsymbol{\Xi}$. The load vector $\mathbf{R}_B$ is the summation of the loads about the B frame origin, including the contributions of gravity load $\mathbf{R}^{\text{grav}}$, inertial load $\mathbf{R}^{\text{iner}}$, induced moment due to tiltrotors $\mathbf{R}^{\text{rate}}$, gyroscopic load $\mathbf{R}^{\text{gyro}}$, and external load $\mathbf{R}^{\text{ext}}$, i.e.,

$$\mathbf{R}_B = \mathbf{R}^{\text{grav}} + \mathbf{R}^{\text{iner}} + \mathbf{R}^{\text{rate}} + \mathbf{R}^{\text{gyro}} + \mathbf{R}^{\text{ext}} \tag{3}$$

The external load includes propulsive and aerodynamic loads, i.e.,

$$\mathbf{R}^{\text{ext}} = \mathbf{R}^{\text{prop}} + \mathbf{R}^{\text{aero}} \tag{4}$$

The aerodynamic load is calculated for each airfoil section along the span of the lifting surfaces (see Fig. 2). The 2-D quasi-steady aerodynamic loads l_{ac}, m_{ac} and d_{ac} on each thin airfoil are determined as functions of trailing-edge flap deflection angle, lifting surface geometry, and

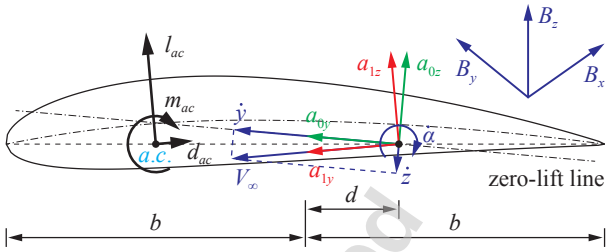

Fig. 2: Aerodynamic frame and load components

acceleration components of Fig. 2 [31]. When gust disturbance is introduced, it is incorporated into the airfoil's local velocity V_∞, thereby modifying the aerodynamic load vector $\mathbf{R}^{\text{aero}}$ to account for the gust effects.

The B frame's orientation is described by the quaternions $\boldsymbol{\zeta}$, governed by

$$\dot{\boldsymbol{\zeta}} = -\frac{1}{2}\boldsymbol{\Omega}_1(\boldsymbol{\omega}_B)\boldsymbol{\zeta} \tag{5}$$

where $\boldsymbol{\Omega}_\zeta$ is a function of the rigid-body angular velocities $\boldsymbol{\omega}_B$. Lastly, the inertial position of the B frame can be calculated by

$$\dot{\mathbf{p}}_B^G = \mathbf{C}^{GB}\mathbf{v}_B = \begin{bmatrix}\mathbf{C}^{GB} & \mathbf{0}_3\end{bmatrix}\boldsymbol{\beta} \tag{6}$$

where $\mathbf{C}^{GB}$ is the rotational transformation matrix from the body to the global frame. The combination of Eq. 2, 5 and 6 completes the nonlinear flight dynamic model of the tiltrotor UAM aircraft. Those equations can be transformed to

$$\begin{aligned}
\dot{\boldsymbol{\beta}} =& \mathbf{M}_{BB}^{-1}\left(-\mathbf{C}_{BB}(\boldsymbol{\beta}, \boldsymbol{\Xi})\boldsymbol{\beta}\right) + \\
& \mathbf{M}_{BB}^{-1}\left(\mathbf{R}_B(\boldsymbol{\beta}, \dot{\boldsymbol{\beta}}, \boldsymbol{\zeta}, \delta_e, \delta_a, \delta_r, \boldsymbol{\Xi}, \dot{\boldsymbol{\Xi}}, \ddot{\boldsymbol{\Xi}}, \dot{\boldsymbol{\Gamma}}, \ddot{\boldsymbol{\Gamma}})\right) \\
\dot{\boldsymbol{\zeta}} =& -\frac{1}{2}\boldsymbol{\Omega}_\zeta(\boldsymbol{\beta})\boldsymbol{\zeta} \\
\dot{\mathbf{p}}_B^G =& \begin{bmatrix}\mathbf{C}^{GB} & \mathbf{0}_3\end{bmatrix}\boldsymbol{\beta}
\end{aligned} \tag{7}$$

where δ_e, δ_a and δ_r are the elevator, aileron, and rudder deflections, $\boldsymbol{\Xi}$ is the vector containing the rotor's tilt angles, and $\boldsymbol{\Gamma}$ is the vector of spin kinematics of the rotors. Therefore, the nonlinear system state and control input vectors are defined as follows,

$$\begin{aligned}
\boldsymbol{x}^T &= \left\{\boldsymbol{\beta}^T\ \dot{\boldsymbol{\beta}}^T\ \boldsymbol{\zeta}^T\ \dot{\boldsymbol{\zeta}}^T\ \left(\mathbf{p}_B^G\right)^T\ \left(\dot{\mathbf{p}}_B^G\right)^T\right\} \\
\mathbf{u}^T &= \left\{\delta_e\ \delta_a\ \delta_r\ \boldsymbol{\Xi}^T\ \dot{\boldsymbol{\Xi}}^T\ \ddot{\boldsymbol{\Xi}}^T\ \dot{\boldsymbol{\Gamma}}^T\ \ddot{\boldsymbol{\Gamma}}^T\right\}
\end{aligned} \tag{8}$$

As a post-processing, the Euler angles can be calculated from the quaternions. By keeping the convention of the Euler angles defined in the north-east-down (NED) frame for flight dynamics, the yaw angle ψ is defined as rotation about negative B_z-axis, the pitch angle θ is defined as rotation about B_x-axis, and the roll angle φ is defined as rotation about B_y-axis. Therefore, the Euler angles are given by

$$\begin{aligned}\varphi &= \tan^{-1}\frac{2\left(\zeta_1\zeta_2-\zeta_0\zeta_3\right)}{1-2\left(\zeta_0^2+\zeta_1^2\right)}\\ \theta &= \sin^{-1}\left[-2\left(\zeta_1\zeta_3+\zeta_0\zeta_2\right)\right]\\ \psi &= \tan^{-1}\frac{2\left(\zeta_0\zeta_1-\zeta_2\zeta_3\right)}{1-2\left(\zeta_1^2+\zeta_2^2\right)}\end{aligned} \tag{9}$$

which can be simply noted as

$$\mathbf{\Phi} = \left\{\varphi\ \theta\ \psi\right\}^T = \mathbf{\Phi}(\boldsymbol{\zeta})\,. \tag{10}$$

Additionally, the system output $\boldsymbol{y}$ can be selected as a combination of system states and Euler angles, with the full form given by

$$\boldsymbol{y}^T = \left\{\boldsymbol{\beta}^T\ \mathbf{\Phi}^T\ \left(\mathbf{p}_B^G\right)^T\right\} \tag{11}$$

3 NONLINEAR MODEL PREDICTIVE CONTROLLER

The nonlinear model predictive controller (NMPC) looks ahead by p steps to predict the system responses in the future (predicted output in Fig. 3). It calculates the best sequence of control inputs $\mathbf{u}$ from the present to $t_n = t + n \times \mathrm{d}t$ to achieve the closest match between the system output and the desired output reference (predicted control input in Fig. 3) [32]. Here, p is the prediction horizon, and n is the control horizon illustrated in Fig. 3. At each time step, the controller predicts the future system output and solves an optimization problem to determine the control input, using only the initial input vector (orange line). This procedure is repeated in the next time step. This approach significantly enhances controller performance with the trade-off of increased computational cost.

In this study, the NMPC is designed using the MATLAB® function *nlmpc*, where the function *nlmpcmove* solves the quadratic problem and find the optimal control input in each time step. The cost function of the quadratic problem is

$$J(\mathbf{U}_k) = J_y(\mathbf{U}_k) + J_u(\mathbf{U}_k) + J_{\Delta u}(\mathbf{U}_k) \tag{12}$$

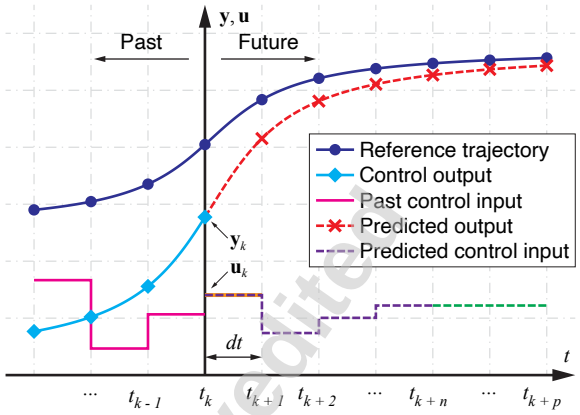

Fig. 3: NMPC control and prediction horizon

where $\mathbf{U}_k$ is the quadratic problem decision defined by

$$\mathbf{U}_k^T = \left\{\mathbf{u}^T(k|k)\ \mathbf{u}^T(k+1|k)\cdots\mathbf{u}^T(k+p-1|k)\right\} \tag{13}$$

The $\mathbf{U}_k^T$ vector contains the inputs vectors $\mathbf{u}^T(k+i-1|k)$ calculated in the current control interval k for the i^{th} prediction horizon step, where i ranges from 1 to the prediction horizon p defined during the controller design. The output reference tracking term J_y given by

$$J_y(\mathbf{U}_k) = \sum_{j=1}^{n_y}\sum_{i=1}^{p}\left\{\frac{w_{i,j}^y}{s_j^y}\left[r_j(k+i|k) - y_j(k+i|k)\right]\right\}^2 \tag{14}$$

relates the j^{th} output reference $r_j(k+i|k)$ to the j^{th} output $y_j(k+i|k)$, both referent to the i^{th} prediction horizon calculated at the current control interval k.The minimization of this term can be tuned by adjusting the weight for j^{th} plant output at the i^{th} prediction horizon step $w_{i,j}^y$ and the scale factor of the j^{th} output s_j^y. The cost function term J_u allows for the input variable tracking and is given by

$$J_u(\mathbf{U}_k) = \sum_{j=1}^{n_u}\sum_{i=0}^{p-1}\left\{\frac{w_{i,j}^u}{s_j^u}\left[u_j(k+i|k) - u_{j,\text{target}}(k+i|k)\right]\right\}^2 \tag{15}$$

where $u_{j,\text{target}}$ is the target value for the j^{th} input. $w_{i,j}^u$ and s_j^u are the weight and the scale factor of the j^{th} input. The

third term of the cost function is

$$J_{\Delta u}(\mathbf{U_k}) = \sum_{j=1}^{n_u} \sum_{i=0}^{p-1} \left\{ \frac{w_{i,j}^{\Delta u}}{s_j^u} \left[u_j(k+i|k) - u_j(k+i-1|k) \right] \right\}^2 \tag{16}$$

which allows for the consideration of input move smoothness during the optimization process.

In the function *nlmpcmove*, the measured disturbances can be inputted as an array of N_{md} (number of measured disturbances) columns and $p+1$ rows to vary the disturbance values over the prediction horizon. When gust excitation is considered, it can be assumed as measured disturbance with known 3D wind speeds throughout the prediction horizon. The measurement of 3D flight speeds ahead in time, and consequently ahead of the aircraft in space, is possible with sensors such as LiDAR [33].

The NMPC is tuned for each case studied by adjusting the output and input weights. Those are considered constant throughout the prediction and control horizons and therefore have the new form w_j^y and w_j^u for the j^{th} output and j^{th} input weights. All the scale factors are chosen as 1, thus are omitted in Eq. 17. The input movement weights $w_{i,j}^{\Delta u}$ are also kept at their default values of 0.1. While the NMPC formulation allows for output constraints, only input and input rate hard constraints are used in this work, i.e.,

$$\begin{aligned} u_{j,\min}(i) &\leqslant u_j(k+i-1|k) \leqslant u_{j,\max}(i) \\ \Delta u_{j,\min}(i) &\leqslant \Delta u_j(k+i-1|k) \leqslant \Delta u_{j,\max}(i) \end{aligned} \tag{17}$$

In addition, this work focuses on NMPC attenuating gust disturbance, thus neglects model uncertainty and other disturbances. In other words, the sensor data is assumed to be perfect reading without the noise on sensor readings.

4 NUMERICAL STUDIES

This study focuses on the NMPC control of a UAM aircraft with six tiltrotors, as shown in Fig. 4. The aircraft's inertial and aerodynamic properties are listed in Tables 1 and 2, respectively. The rigid propeller pylon length is assumed to be 1 m. A comprehensive trim analysis at multiple flight conditions and the validation of the rotor tilt transition flight were investigated in a previous study (Ref. [31]) and will not be discussed here. The results showed that the aircraft model studied is stable and

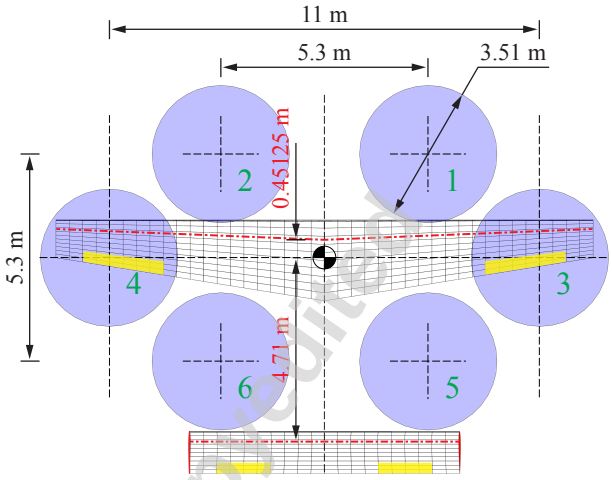

Fig. 4: Tiltrotor UAM aircraft geometry and rotor positions

Table 1: Inertial properties of UAM aircraft

Inertial Property	Value	Unit
Body mass, m_B	2,240.73	kg
Body moment of inertia, $I_{B,xx}$	12,000	$\text{kg}\,\text{m}^2$
Body moment of inertia, $I_{B,yy}$	9,400	$\text{kg}\,\text{m}^2$
Body moment of inertia, $I_{B,zz}$	20,000	$\text{kg}\,\text{m}^2$
Rotor mass, m_r	4.55	kg
Rotor moment of inertia, $I_{r,xx}^e$	3.5	$\text{kg}\,\text{m}^2$
Rotor moment of inertia, $I_{r,yy}^e$	7.0	$\text{kg}\,\text{m}^2$
Rotor moment of inertia, $I_{r,zz}^e$	3.5	$\text{kg}\,\text{m}^2$

that the formulation can capture the essential characteristics of rotor kinematics, such as tilt angle and spin rate, regarding the overall vehicle response.

The vehicle is first brought to a trimmed flight condition with a level flight speed of $68\,\text{m}\,\text{s}^{-1}$ due North and an altitude of $304.8\,\text{m}$ due north. This corresponds to a tip Mach number of 0.2 and a wing tip unit Reynolds number of $3.8 \times 10^6\ \text{m}^{-1}$. The chosen configuration has a lower flight speed and altitude than other similar aircraft in the literature [34, 35]. In [34], a tiltrotor UAM aircraft operated at flight speeds of $168\,\text{m}\,\text{s}^{-1}$ and a cruise altitude of $3000\,\text{m}$ above sea level, resulting in a tip Mach of 0.48 and a tip unit Reynolds number of $8.99 \times 10^6\ \text{m}^{-1}$. The lower speed and altitude is selected in this work to con-

Table 2: Aerodynamic properties of UAM aircraft

Aerodynamic Property	Wing	Tail
Airfoil	NACA 0012	NACA 0012
Ref. axis location *	25%	25%
Span, m	13.72	6.90
Sweep angle, deg	-2.306	0
Dihedral angle, deg	0	0
Chord (root/tip), m	2.075/0.970	1.080/1.080
Incidence angle, deg **	3.1598	1.0626

* From leading-edge

** Incident angle with no twist

sider the critical case of flying in a city setting closer to buildings and other obstacles.

For all cases, the NMPC input is the increment along a time step ($\Delta\mathbf{u}$), as shown in

$$\begin{aligned}\Delta\mathbf{u}(k) &= \mathbf{u}(k) - \mathbf{u}(k-1)\\ \Delta\mathbf{u}_{\text{target}}(k+1) &= \mathbf{u}_{\text{target}}(k) - \mathbf{u}(k)\end{aligned} \tag{18}$$

The input target for $\Delta\mathbf{u}$ is the difference between the desired input at the current time step and the current input vector ($\Delta\mathbf{u}_{\text{target}}$). When the input is equal to the target, $\Delta\mathbf{u}_{\text{target}}$ equals zero. Minimizing the difference between $\Delta\mathbf{u}$ and $\Delta\mathbf{u}_{\text{target}}$ in the NMPC cost function consists of making the input equal to the target while leading to a constant condition ($\mathbf{u}(k) = \mathbf{u}(k-1)$). This approach eliminates the impact of input scale on the cost function minimization. For instance, when using $\Delta\mathbf{u}$, the difference in scale between elevator (0.01) and rotor spin rate inputs (3000) does not significantly affect the cost function minimization.

The states $\mathbf{x}$ and output $\mathbf{y}$ are given by

$$\begin{aligned}\mathbf{x}^T &= \left\{\boldsymbol{\beta}^T \ \boldsymbol{\zeta}^T \ \left(\mathbf{p}_B^G\right)^T\right\}\\ \mathbf{y}^T &= \left\{\phi \ \theta \ \psi \ p_{B,x}^G \ p_{B,y}^G \ p_{B,z}^G\right\}\end{aligned} \tag{19}$$

where ϕ, θ, and ψ are the roll, pitch, and yaw angles in degrees. $p_{B,x}^G$, $p_{B,y}^G$ and $p_{B,z}^G$ are the B's frame inertial position measured in meters.

The following gust excitation cases are investigated:

- Continuous stochastic gust (Sect. 4.1)

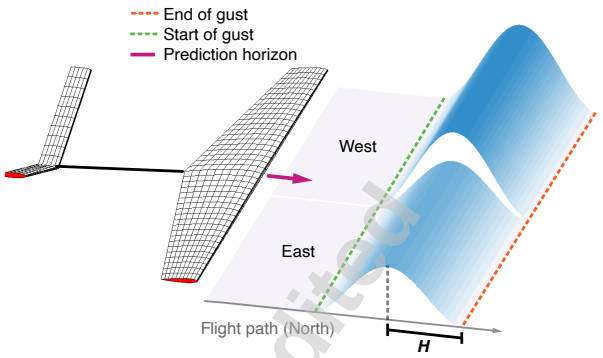

Fig. 5: Discrete gust excitation diagram

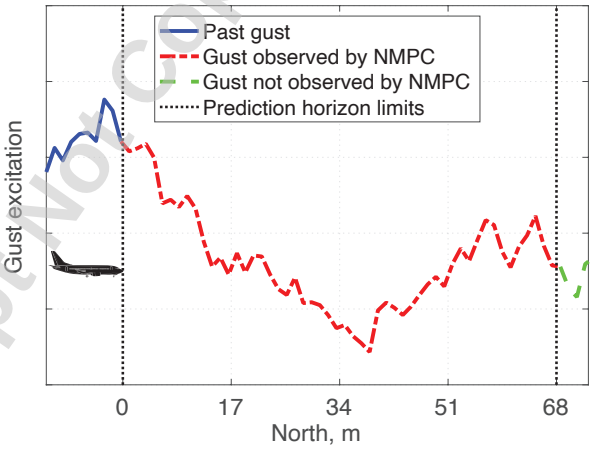

Fig. 6: Diagram of gust excitation observed by NMPC. Airplane representation approximated eVTOL aircraft length of 5.9 meters

- Discrete gust (Sect. 4.2)

Fig. 5 illustrates the gust excitation for the discrete gust case. This diagram also applies to the continuous gust but with a different gust profile. The gust magnitude varies in the level flight path direction (North). Both continuous and discrete gusts are assessed with gust excitation applied symmetrically and asymmetrically to the lifting surfaces of the aircraft. In the symmetric case, the gust magnitude remains constant along the wing span. In the asymmetric case, the right wing and tail are subject to the gust with a 80 % magnitude of the nominal one, as shown in Fig. 5.

In addition, the gust velocity profile along the prediction horizon can be fed to the NMPC, allowing it to predict a more accurate dynamic response and find a more robust control for the aircraft. In order to simplify the

study, the gust magnitude at the wing root V_{w} (middle of the aircraft) is provided to the NMPC as the measured disturbance. This setup is feasible in practice as one can use a LiDAR sensor to measure the gust component down the path. In this study, the gust profile in the range of $68\,\mathrm{m}$ ahead of the aircraft is used in the NMPC, as shown in Fig. 6. This is equivalent to a prediction horizon of $1\,\mathrm{s}$, as the nominal flight speed of the aircraft is $68\,\mathrm{m\,s^{-1}}$.

The control input vector consists of

$$\mathbf{u}^T = \left\{\Delta\delta_e \ \Delta\delta_a \ \Delta\delta_r \ \Delta\dot{\Gamma}_3 \ \Delta\dot{\Gamma}_4\right\} \tag{20}$$

where $\dot{\Gamma}_3$ and $\dot{\Gamma}_4$ are the spin rates of rotors 3 and 4, respectively. Note that rotors 3 and 4 are used as thrusters with no tilt commanded. The goal of the NMPC is to minimize the path deviation caused by gust excitation and regulate the aircraft to its trimmed flight condition. For this purpose, the input target $\mathbf{u}_{\text{target}}$ in Eq. 18 is the trimmed flight input condition. Additionally, the reference output $\mathbf{y}_{\text{ref}}$ is the initial output vector.

The case ID convention used here follows the format "1-23-4". "1" describes whether the simulation is open-loop (O) or NMPC (N). "2" indicates the type of gust excitation, with S for continuous stochastic gust and D for discrete gust. "3" provides information on whether the gust was applied symmetrically (S) or asymmetrically (A) to the aircraft lifting surfaces. Lastly, "4" gives additional details such as gust turbulence intensity for continuous gust case and gust maximum vertical speed for discrete gust case. Table 3 shows the case IDs and descriptions for all simulations presented in this section. Detailed information on open loop and controller settings can be found in Appendix A. For all cases, the NMPC is simulated using a time step of $0.1\,\mathrm{s}$, and *fmincon* as the optimization problem solver from MATLAB's Optimization Toolbox.

Table 3: Case ID and descriptions

Case ID	Description
O-SS-41	OPEN - sym. turbulence σ_{w} of $4.1\,\mathrm{m\,s^{-1}}$
N-SS-41	NMPC - sym. turbulence σ_{w} of $4.1\,\mathrm{m\,s^{-1}}$
N-SS-46	NMPC - sym. turbulence σ_{w} of $4.6\,\mathrm{m\,s^{-1}}$
N-SS-51	NMPC - sym. turbulence σ_{w} of $5.1\,\mathrm{m\,s^{-1}}$
N-SS-56	NMPC - sym. turbulence σ_{w} of $5.6\,\mathrm{m\,s^{-1}}$
O-SA-41	OPEN - asym. turbulence σ_{w} of $4.1\,\mathrm{m\,s^{-1}}$
N-SA-41	NMPC - asym. turbulence σ_{w} of $4.1\,\mathrm{m\,s^{-1}}$
N-SA-46	NMPC - asym. turbulence σ_{w} of $4.6\,\mathrm{m\,s^{-1}}$
N-SA-51	NMPC - asym. turbulence σ_{w} of $5.1\,\mathrm{m\,s^{-1}}$
O-DS-17	OPEN - sym. discrete, V_{max} of $16.8\,\mathrm{m\,s^{-1}}$
N-DS-02	NMPC - sym. discrete, V_{max} of $1.52\,\mathrm{m\,s^{-1}}$
N-DS-07	NMPC - sym. discrete, V_{max} of $6.62\,\mathrm{m\,s^{-1}}$
N-DS-12	NMPC - sym. discrete, V_{max} of $11.73\,\mathrm{m\,s^{-1}}$
N-DS-17	NMPC - sym. discrete, V_{max} of $16.8\,\mathrm{m\,s^{-1}}$
O-DA-07	OPEN - asym. discrete, V_{max} of $6.62\,\mathrm{m\,s^{-1}}$
N-DA-02	NMPC - asym. discrete, V_{max} of $1.52\,\mathrm{m\,s^{-1}}$
N-DA-07	NMPC - asym. discrete, V_{max} of $6.62\,\mathrm{m\,s^{-1}}$
N-DA-12	NMPC - asym. discrete, V_{max} of $11.73\,\mathrm{m\,s^{-1}}$
N-DA-17	NMPC - asym. discrete, V_{max} of $16.8\,\mathrm{m\,s^{-1}}$

OPEN: Open loop response, i. e. no controller

σ_{w}: Vertical turbulence gust intensity

V_{max}: Maximum discrete gust velocity

4.1 Continuous Stochastic Gust

The gust model Dryden wind Turbulence Model of the Military Specification MIL-F-8785C is used, where the turbulence is formulated as a stochastic process defined by velocity spectra [36]. This study assumes a purely vertical gust with velocity spectra given by

$$\Phi_{\mathrm{w}}(\omega) = \frac{\sigma_{\mathrm{w}}^2 L_{\mathrm{w}}}{\pi V} \times \frac{1 + 3\left(L_{\mathrm{w}}\frac{\omega}{V}\right)^2}{\left[1 + (L_{\mathrm{w}}\frac{\omega}{V})^2\right]^2} \tag{21}$$

where σ_{w} is the vertical turbulence intensity, L_{w} is the turbulence scale length, V is the aircraft flight speed through a frozen turbulence field, and ω is the frequency, with value inside a user-determined range. The gust velocity spectra with turbulence intensity of $4.1\,\mathrm{m\,s^{-1}}$ is presented in Fig. 7. For altitudes below or equal to $304.8\,\mathrm{m}$, which is the case assumed in this work, the turbulence scale length L_{w} is equal to the altitude and the vertical turbulence intensity σ_{w} is equal to $10\,\%$ of the wind speed at $6\,\mathrm{m}$ altitude ($\sigma_{\mathrm{w,6}}$). The settings used for the Dryden gusts are presented in Table 4. The four different intensity values σ_{w} presented are used, creating stochastic gusts of different intensities to evaluate the limits of the NMPC capabilities.

The gust time history is calculated using the inverse Fourier theory. The gust vertical component for each time

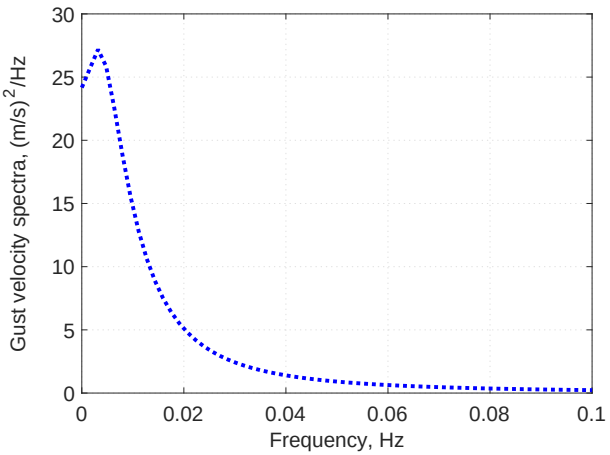

Fig. 7: Stochastic gust velocity spectra with turbulence intensity of 4.1 m/s

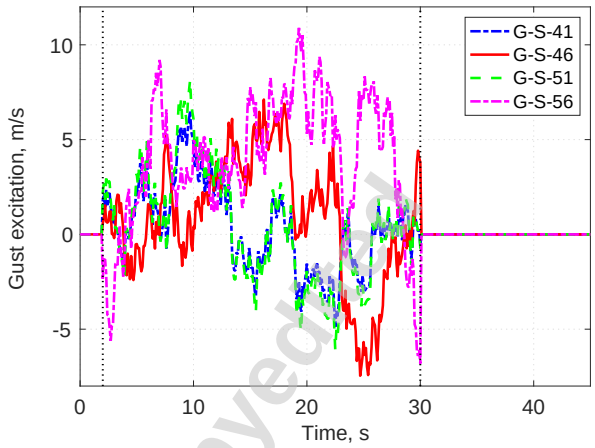

Fig. 8: Stochastic gust excitation for different turbulence intensities

Table 4: Dryden Turbulent gust setting.

Parameter	Value	Unit
Vertical turbulence intensity σ_{w}	4.1, 4.6, 5.1, 5.6	$\mathrm{m\,s^{-1}}$
Turbulence scale length L_{w}	304.8	m
Flight speed V	68	$\mathrm{m\,s^{-1}}$
Frequency range $\{0, \omega_{\mathrm{max}}\}$	$\{0, 10\}$	Hz
Frequency step $\Delta\omega$	0.06	$\mathrm{rad\,s^{-1}}$

step is given by

$$V_{\mathrm{w,c}}(t) = \sum_{i=0}^{\omega_{\mathrm{max}}} \left(\sqrt{\Phi_{\mathrm{w}}(\omega_i)\Delta\omega}\, \cos\left(\omega_i t + \Psi\right) \right) \tag{22}$$

where $\Delta\omega$ is the frequency step and Ψ is a random phase shift in rad. The frequencies evaluated are defined by the desired frequency range going from 0 to ω_{max} (see Table 4).

During the simulation, the system is subjected to continuous gust excitation from 2 to 30 s. The gust signals of the four vertical turbulence intensities mentioned in Table 4 are shown in Fig. 8. These gust profiles, given as vertical velocity in the global coordinate system G, are converted to the body-fixed frame B and added to local velocity calculated for the airfoil sections along the wing/tail span $\dot{\mathbf{p}}_{\mathrm{w}}$ as follows

$$V_\infty = \dot{\mathbf{p}}_{\mathrm{w}} - \mathbf{C}^{BG} \begin{Bmatrix} 0 \\ 0 \\ V_{\mathrm{w}} \end{Bmatrix} \tag{23}$$

where $\mathbf{C}^{BG}$ is the rotational transformation matrix from the global to body frame and V_∞ is the air speed in the airfoil section of Fig. 2.

As seen in Fig. 5, the tail is expected to encounter the gust after the wing. Therefore, the distance from the wing and tail is taken into consideration when determining the gust excitation on the tail nodes. First, the distance between tail and wing nodes in the North direction Δy_{tail} is determined to be $5.16\,\mathrm{m}$ in the wing root. This distance is then converted to time by the following operation

$$t_{\mathrm{tail}} = t - \frac{\Delta y_{\mathrm{tail}}}{\dot{p}^G_{B,y}} \tag{24}$$

where t is the current simulation time used to determine the wing's gust excitation and $\dot{p}^G_{B,y}$ is the north-wise aircraft velocity. A linear interpolation is used to find the tail gust excitation corresponding to t_{tail} for the simulation time step t_k

$$\begin{aligned} V_{\mathrm{tail}}(t_k) = {} & V_{\mathrm{w}}(t_{k-1}) \\ & + \frac{V_{\mathrm{w}}(t_k) - V_{\mathrm{w}}(t_{k-1})}{t_k - t_{k-1}} \times (t_{\mathrm{tail}} - t_{k-1}) \end{aligned} \tag{25}$$

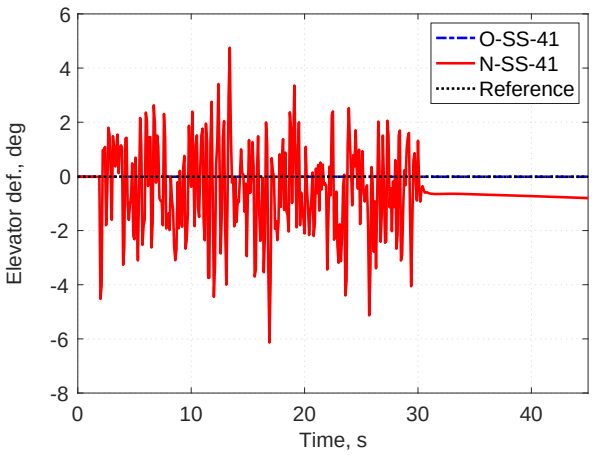

Fig. 9: Elevator input during flight under symmetric stochastic gust excitation with turbulence intensity of 4.1 m/s

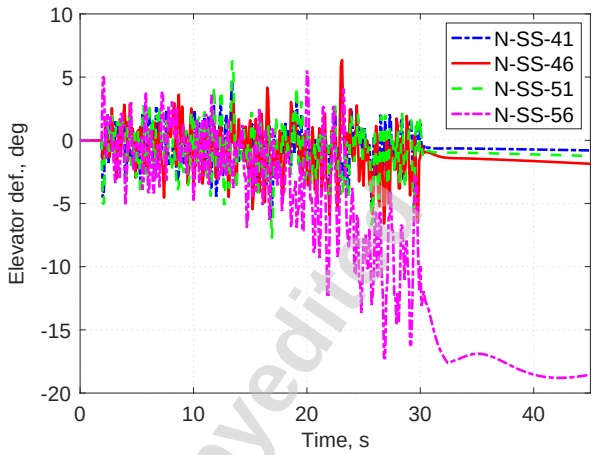

Fig. 10: Elevator input during flight under symmetric stochastic gust excitation with different turbulence intensities

whose value is subtracted from $\dot{\mathbf{p}}_w$ of the airfoil sections along the tail span according to Eq. 23.

4.1.1 *Symmetric Stochastic Gust*

The symmetric stochastic gust involves aircraft experiencing the gust excitations of Fig. 8 equally affecting both the right and left-hand sides of the aircraft lifting surfaces. This symmetric gust results in longitudinal aircraft motion, causing changes in altitude and pitch angle. Figs. 11 and 9 display the results for aircraft flight with and without the designed NMPC controller for path correction when subjected to a gust intensity of $\sigma_w = 4.1\,\mathrm{m\,s^{-1}}$. The NMPC's objective is to maintain the trimmed flight condition by keeping the system outputs constant at their initial values. The NMPC output weight for $p^G_{B,y}$ is set to zero (refer to Appendix A) to exclude its values from the NMPC optimization process. The NMPC primarily controls the longitudinal flight using elevator deflection as input. The elevator input rate allowed is $50\,\mathrm{deg/s}$, which is conservative when compared to the literature that reports deflection speeds of $70\,\mathrm{deg/s}$ or higher [37].

Fig. 11 illustrates the pitch angle and flight path of the aircraft. The open loop results show a significant deviation from the intended path. However, with the assistance of the controller, the aircraft can maintain a near-constant altitude while deviating from the desired pitch angle only during gust excitation. While the NMPC achieves good path tracking, the results indicate that the optimal solution found by the NMPC differs from the initial condition. Before the gust encounter, the aircraft is trimmed with a zero pitch angle at the altitude of $304.8\,\mathrm{m}$, achieved with an elevator deflection of -0.013 deg. After the aircraft hits the gust, the NMPC identifies a new optimal condition consisting of a near-constant pitch angle of $0.5\,\mathrm{deg}$, resulting from an elevator deflection of -0.8 deg. This response highlights that the gust perturbation caused a shift in the trim condition, forcing the controller to prioritize either orientation or position tracking but not both simultaneously.

The NMPC's limitations are explored by analyzing the effects of increasingly intense gusts, with performance results shown in Figs. 10 and 12. These results demonstrate that the NMPC can maintain control of the flight path for gust intensities up to $5.1\,\mathrm{m\,s^{-1}}$. In these cases, the NMPC handles the disturbances with only minor deviations in pitch angle and elevator input, which stabilize soon after the gust has passed. However, when gust intensity is raised to $5.6\,\mathrm{m\,s^{-1}}$, the NMPC reaches the ceiling of its control capabilities. This loss of control is evidenced by an increase in pitching oscillation magnitude while the gust is active, along with a substantial decrease in altitude immediately following the gust disturbance. The elevator deflection angle also exhibits a progressive oscillation with growing amplitude, suggesting that while the NMPC attempts to control the flight path, it requires increasingly high control inputs to counteract the instability introduced by the gust. When the gust excitation is abruptly removed, the NMPC can no longer effectively correct the flight path.

The challenge of controlling an aircraft during intense turbulence is better illustrated by Fig. 13, which

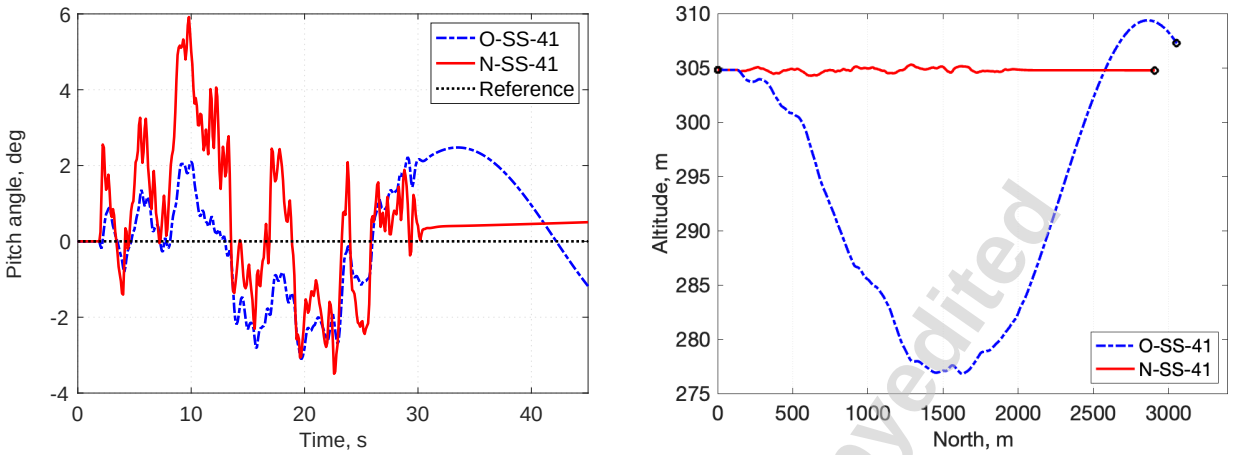

Fig. 11: Pitch angle and aircraft trajectory response during flight under symmetric stochastic gust excitation with turbulence intensity of 4.1 m/s

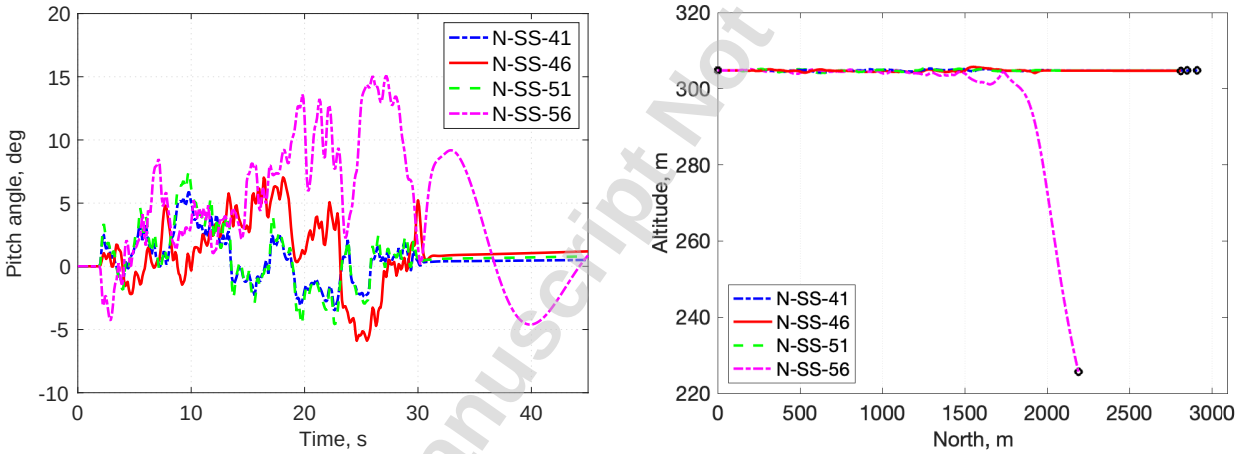

Fig. 12: Pitch angle and aircraft trajectory response during flight under symmetric stochastic gust excitation with different turbulence intensities

shows the pitch angle rate and vertical body velocity for different turbulence intensities. The results indicate that the vertical velocity reaches higher magnitudes after the gust excitation, as a result of the loss of control by the NMPC at that moment. The main cause of this loss of control is the pitch angle rate, which shows an increase in magnitude prior to that instant, reaching its maximum at 25 s. Although the NMPC indirectly addresses these issues by maintaining the pitch angle and vertical position, it does not directly track the pitch angle rate or the vertical velocity as they are not part of the output vector. Adding the pitch angle rate as a system output could potentially help improve the control of the aircraft in challenging gust conditions. However, this addition would also increase the complexity of control, introducing another variable into the optimization problem and consequently increasing the computational cost.

4.1.2 *Asymmetric Stochastic Gust*

For the asymmetric gust study, a gust with the nominal magnitude is applied to the left wing and tail, while the right lifting surfaces are subjected to a gust with 80% of the nominal magnitude (see Fig. 5). As a result, the flight path is expected to deviate from the desired trimmed flight path in both the longitudinal and lateral directions. Therefore, the NMPC needs to utilize all available control inputs to control both motions and maintain the aircraft

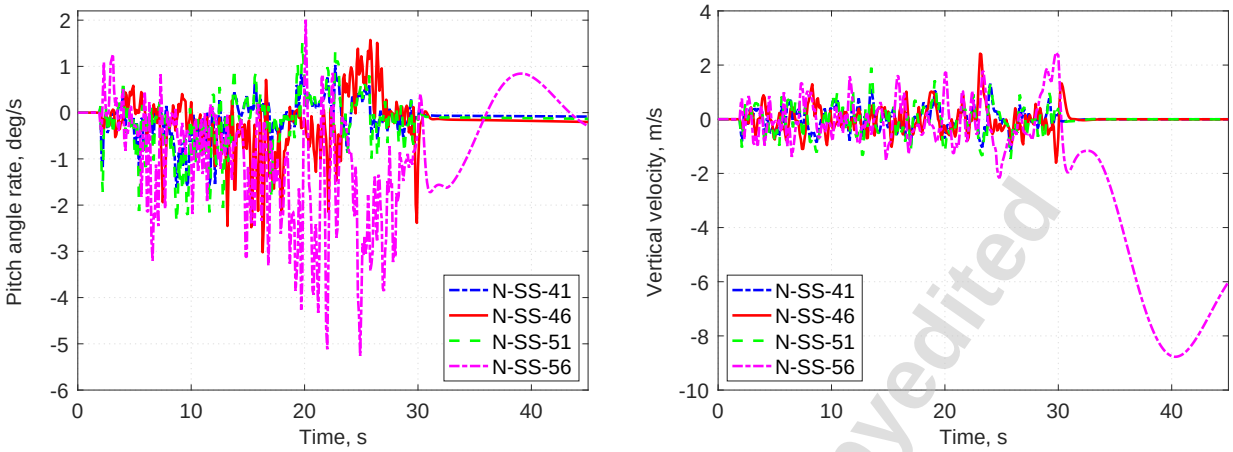

Fig. 13: Pitch angle rate and vertical body velocity during flight under symmetric stochastic gust excitation with different turbulence intensities

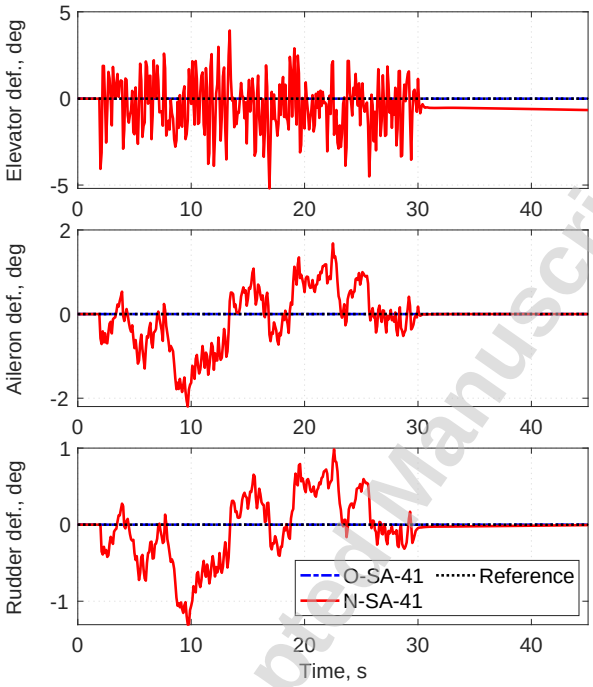

Fig. 14: Control surfaces inputs during flight under asymmetric stochastic gust excitation with turbulence intensity of 4.1 m/s

on its intended path. The control surface inputs, Euler angle system response and the flight path for both open loop and NMPC with turbulence intensity of $4.1\,\mathrm{m\,s^{-1}}$ are presented in Figs. 14-16.

The open-loop response shows that the asymmetric stochastic gust excitation causes the aircraft to lose altitude while turning due east, caused by the higher gust excitation happening on the left side of the aircraft. Such a response is not observed in the case with a flight controller, where level flight is maintained, showing only small oscillations of pitch angle during gust excitation. These oscillations are completely suppressed after the gust ends. Since there is now a lateral motion component, both aileron and rudder inputs are used in addition to the elevator, all with reasonable input magnitudes. More specifically, the elevator is used by the NMPC for altitude and pitch control, and the aileron and rudder for roll angle, yaw angle, and lateral path control. Again, different trim conditions are observed before and after the gust disturbance, with the main deviation occurring in the pitch angle. When flying with calm air, the aircraft's Euler angle components are all zeros at the altitude of $304.8\,\mathrm{m}$, achieved with an elevator deflection of $-0.013\,\mathrm{deg}$ and no input from the aileron or rudder. After the gust disturbance, the roll and yaw angles remain near zero, but the pitch angle shifts to $0.42\,\mathrm{deg}$ at the same altitude, resulting from approximately zero aileron and rudder deflections and an elevator deflection of $-0.67\,\mathrm{deg}$.

The controller is further examined by simulating the cases with higher-intensity gusts. The results are compared in Figs. 19 and 18 for the system subjected to the control surface inputs of Fig. 17. The increase in path deviation observed is not linear with the increase in gust intensity because the turbulent time domain curves are not the same with only magnitude change. The profile of the gust velocities, particularly the values close to the end of gust excitation, directly affects the aircraft's flight

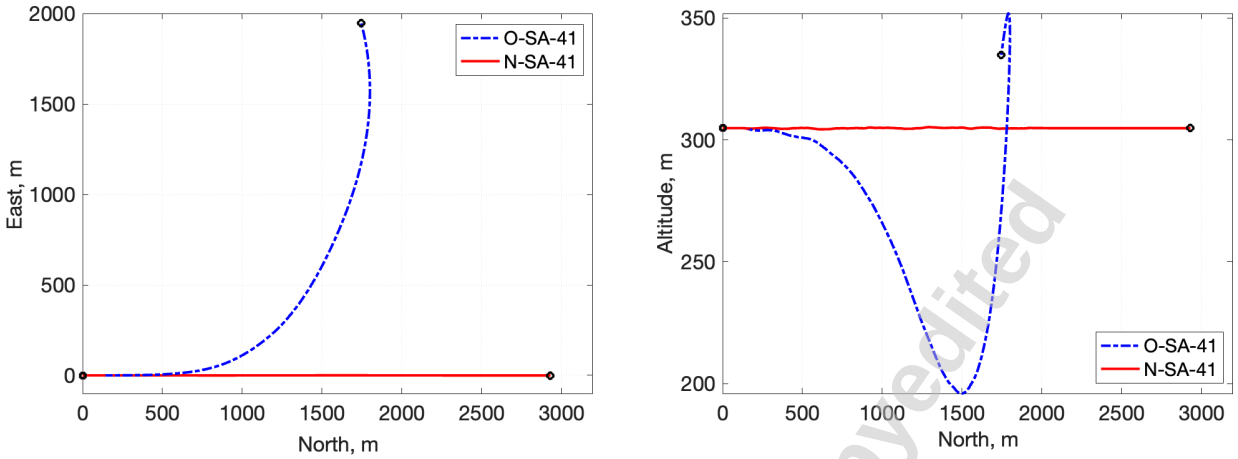

Fig. 15: Aircraft trajectory response during flight under asymmetric stochastic gust excitation with turbulence intensity of 4.1 m/s

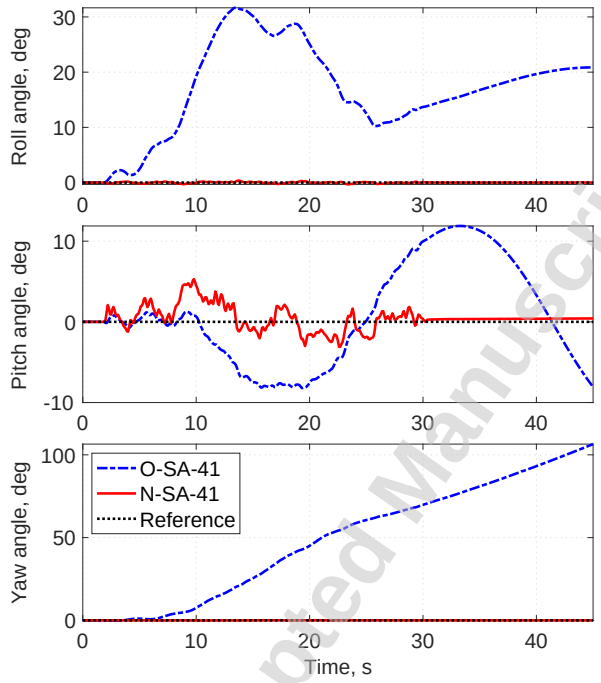

Fig. 16: Euler angle response during flight under asymmetric stochastic gust excitation with turbulence intensity of 4.1 m/s

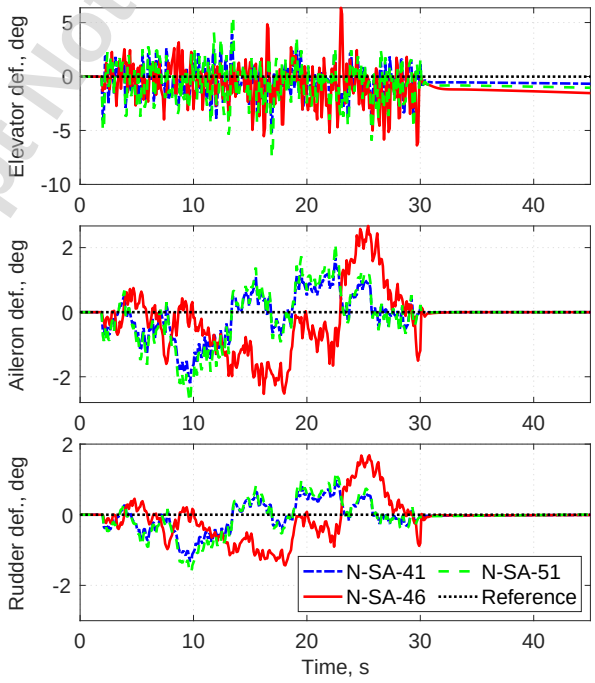

Fig. 17: Control surfaces inputs during flight under asymmetric stochastic gust excitation with different turbulence intensities

path after the gust disappears. The results indicate that the aircraft's lateral position is primarily affected by the different gust intensities. In addition, the aircraft drifts down after the gust excitation in all cases, with a greater deviation for the gust with higher intensities. However, even for the high gust intensity considered (5.1 $\mathrm{m\,s^{-1}}$), the flight is still controllable.

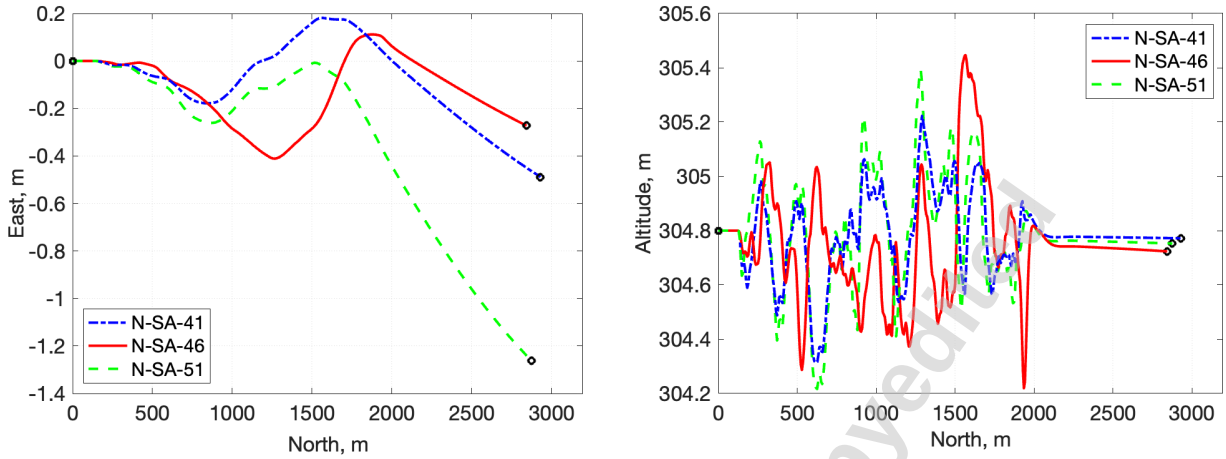

Fig. 18: Aircraft trajectory response during flight under asymmetric stochastic gust excitation with different turbulence intensities

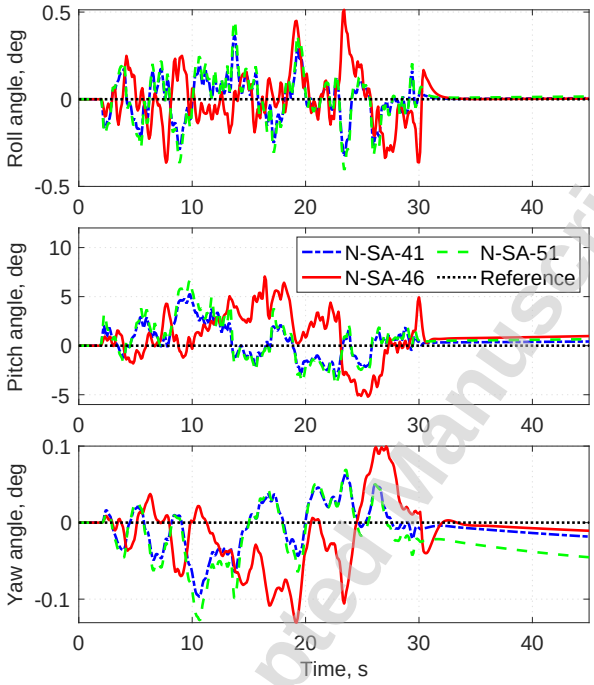

Fig. 19: Euler angle response during flight under asymmetric stochastic gust excitation with different turbulence intensities

4.2 Discrete "1-cosine" Gust

The discrete gust used has a "1-cosine" shape in accordance to [36] and is given by

$$V_{\mathrm{w},d}(p^G_{B,y}) = \frac{V_{\max}}{2}\left[1-\cos\left(\frac{\pi(p^G_{B,y}-p^G_{B,y0})}{H}\right)\right] \tag{26}$$

where $V_{\mathrm{w},d}$ is the gust vertical component for a specific northward position $p^G_{B,y}$. $p^G_{B,y0}$ is the initial y-coordinate when the aircraft encounters the gust indicated by the green dotted line in Fig. 5. The variable H denotes the gust gradient, which is equal to half the width of the gust wave (see Fig. 5). The literature recommends the investigation of gust gradients ranging from 9.14 to $106.7\,\mathrm{m}$ to determine the critical gust width [36]. Upon investigation, the case with the larger open-loop deviations is found to be the $106.7\,\mathrm{m}$ case, which will be used from now on. $V_{\max}$ represents the design gust velocity, which can be calculated based on a reference gust velocity associated with the flight airspeed, as well as the flight profile alleviation factor derived from flight altitude and aircraft weight information. However, in this study, $V_{\max}$ is used as a parameter to define the discrete gust intensity curve, as it is equal to the gust magnitude at the peak of the curve.

The discrete gust settings are detailed in Table 5. The gust is expected to first interact with the aircraft at $136\,\mathrm{m}$ north, which is anticipated to occur $2\,\mathrm{s}$ into the simulation, assuming a constant flight speed of $68\,\mathrm{m\,s^{-1}}$. The

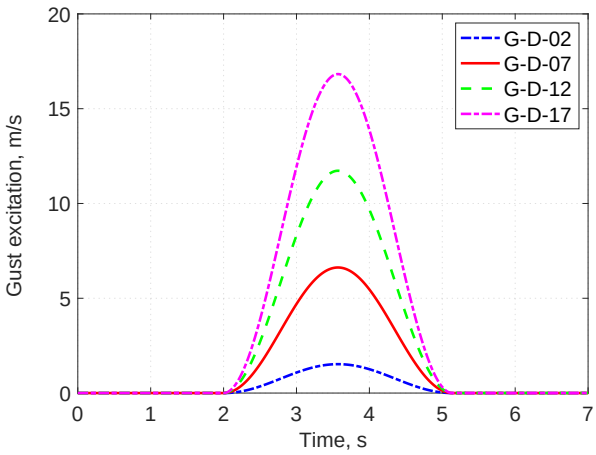

Fig. 20: Discrete gust excitation for different 1-cos curve intensities

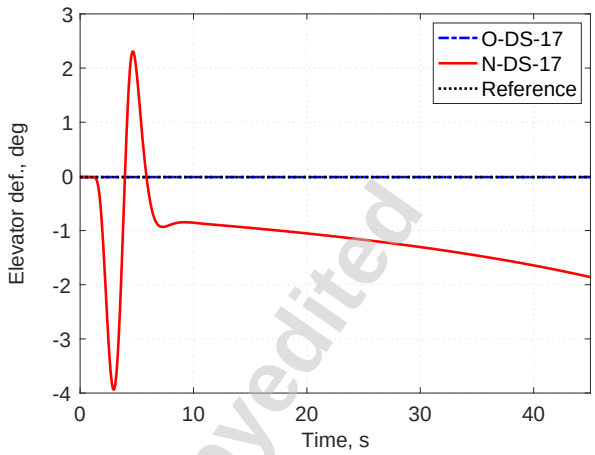

Fig. 21: Elevator input during flight with 16.8 m/s maximum magnitude symmetric discrete gust excitation

Table 5: Discrete 1-cos gust setting.

Parameter	Value	Unit
Maximum gust velocity $V_{\max}$	1.52, 6.62, 11.73, 16.8	$\mathrm{m\,s^{-1}}$
Gust gradient H	106.7	m
Location of gust start $p^G_{B,y0}$	136	m

resulting gust curves for the four maximum gust velocities mentioned in Table 5 are shown in Fig. 20. Table 3 summarizes the case IDs and descriptions discussed in this section with detailed NMPC settings presented in Appendix A.

The discrete gust curves shown in Fig. 20 are subtracted from $\dot{\mathbf{p}}_{\mathrm{w}}$ of the airfoil sections along the wing/tail span according to Eq. 23. Similar to before, the gust excitation at the tail nodes is calculated taking into account the distance of the tail nodes to the wing root, denoted as Δy_{tail}. The discrete gust excitation described in Eq. 26 depends on the north aircraft position $p^G_{B,y}$. Therefore, simplifying the determination of the tail gust can be achieved by substituting $p^G_{B,y}$ in Eq. 26 with the north position of the tail, given by

$$p^G_{B,y,\mathrm{tail}} = p^G_{B,y} - \Delta y_{\mathrm{tail}} \tag{27}$$

where the distance of the tail nodes to the wing root $\Delta y_{\mathrm{tail}} = 5.16\,\mathrm{m}$ and $p^G_{B,y}$ is the northward position of the aircraft wing root in the global frame.

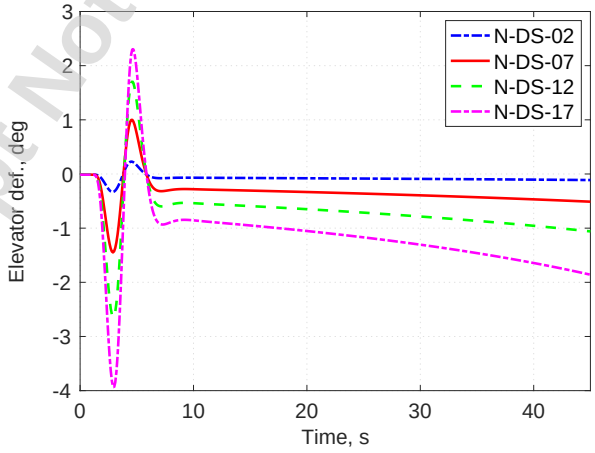

Fig. 22: Elevator input during flight with symmetric discrete gust excitation for different maximum magnitudes

4.2.1 *Symmetric Discrete Gust*

The gust excites the lifting surfaces of the aircraft equally on both sides, resulting in a longitudinal aircraft motion that must be controlled by the NMPC, similar to the case discussed in Sect. 4.1.1.

The results for the open loop and NMPC simulations are compared in Figs. 21 and 23 for the case with a maximum gust velocity of $16.8\,\mathrm{m\,s^{-1}}$. The open loop response shows oscillation of both pitch angle and altitude caused by the gust excitation, which is not suppressed by the end of the simulation. On the other hand, the close loop simulation with NMPC can maintain a nearly constant altitude with a slight oscillation of altitude during gust ex-

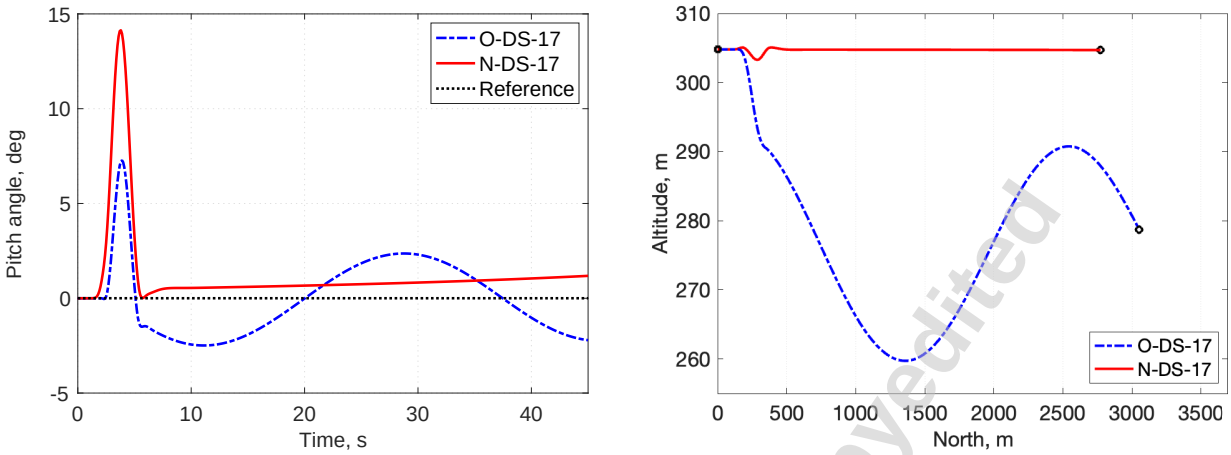

Fig. 23: Pitch angle and aircraft trajectory response during flight with 16.8 m/s maximum magnitude symmetric discrete gust excitation

citation. However, Fig. 21 shows a gradual increase in the elevator input magnitude after gust excitation, reaching -1.86 deg by the end of the simulation. This results in a steady increase in the pitch angle, reaching 1.18 deg at the end of the simulation. Additionally, the pitch angle deviation during gust excitation is higher than the open-loop response. The non-constant elevator input and the resulting pitch angle response after excitation indicate that, while the controller successfully maintains a constant altitude, the aircraft does not return to the initial pitch angle or achieve a stable input/output condition, meaning the trimmed flight is not re-established.

The gust intensity is reduced to determine if a less severe gust leads to less deviation in pitch angle and elevator input. That is what is observed in Figs. 22 and 24, which compares the controller results for the gust intensities mentioned in Table 5. However, even with a small gust magnitude of $1.52\,\mathrm{m\,s^{-1}}$, some deviation is still observed. The results indicate that gust intensity has a more significant influence on pitch angle control compared to altitude. This is because the altitude deviation from the path shows minimal changes for the different gust intensity cases.

4.2.2 *Asymmetric Discrete Gust*

In order to study the effects of uneven discrete gusts on NMPC effectiveness, the left wing and tail sides experience full gusts, while the right side experiences 80% of the gust velocity, similar to the asymmetric stochastic gust discussed in Sect. 4.1.2. This is expected to cause the aircraft to deviate from its intended flight path in both longitudinal and lateral planes, which must be controlled by the NMPC. The NMPC takes advantage of all control surfaces to do so (Fig. 25). Once again, the elevator input does not return to its initial value. Instead, it exhibits a gradual increase in magnitude, ultimately reaching -0.45 deg. This behavior is not observed for the aileron and is only observed to a lesser extent for the rudder, which reaches -0.03 deg. Although the pitch angle deviates from its initial value after gust excitation (initially zero), reaching 0.28 deg (see Fig. 26), the aircraft maintains a nearly constant flight path, as illustrated in Fig. 27, with a minimal East position deviation of 1.23 m by the end of the flight.

When comparing the responses for different gust excitation magnitudes (Figs. 28 to 30), the results show that an increase in gust excitation causes an increase in pitch and yaw angle deviations after gust excitation. Consequently, a deviation of lateral position and altitude is also observed, showing that a level flight was not achieved. Even with such deviation, the NMPC greatly improves the stability and path tracking for the aircraft compared to the open loop response.

5 CONCLUSION AND FUTURE WORK

This paper presented the implementation of a Nonlinear Model Predictive Controller (NMPC) for an urban air mobility aircraft during level flight under gust excitation. The performance of the NMPC was assessed for continuous stochastic and discrete "1-cosine" gust control. In both cases, the gust was applied symmetrically to both sides of the aircraft's lifting surfaces (symmetric gust) and with a higher intensity on the left side (asymmetric gust). The findings showed that the NMPC effectively

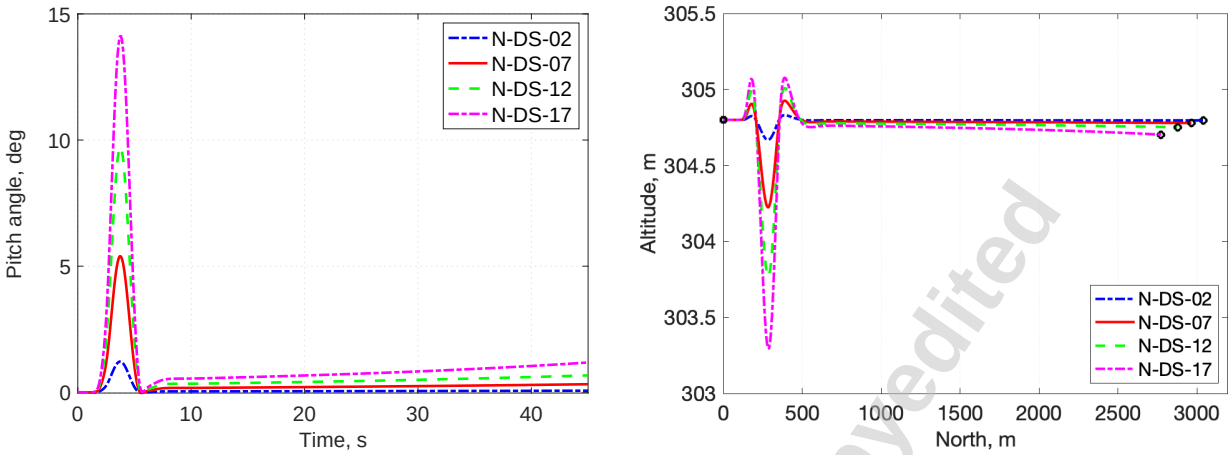

Fig. 24: Pitch angle and aircraft trajectory response during flight with symmetric discrete gust excitation for different maximum magnitudes

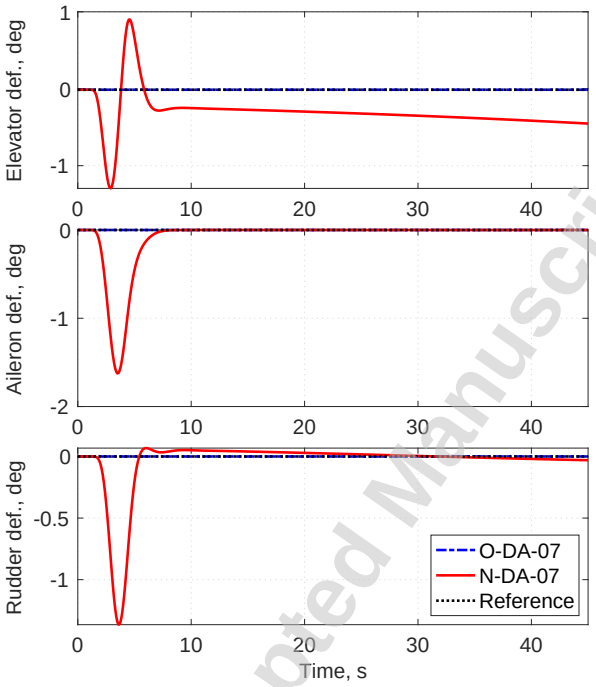

Fig. 25: Control surfaces inputs during flight with 6.62 m/s maximum magnitude asymmetric discrete gust excitation

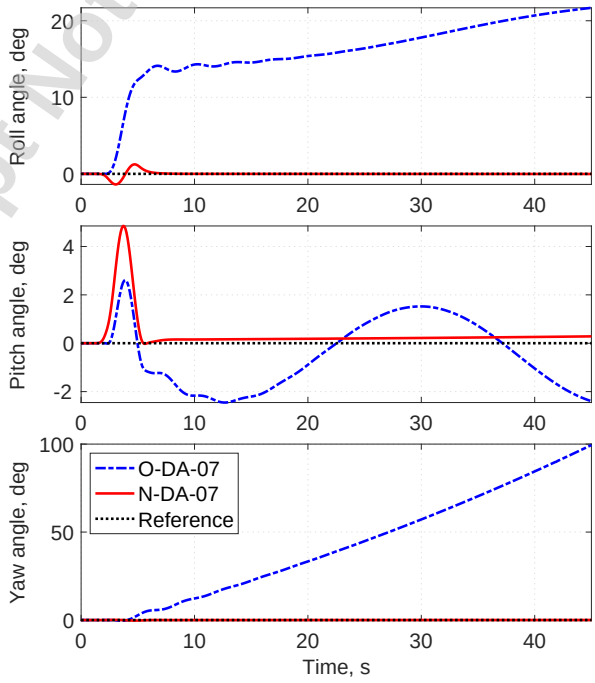

Fig. 26: Euler angle response during flight with 6.62 m/s maximum magnitude asymmetric discrete gust excitation

minimized flight path deviation caused by the stochastic gust for turbulence intensity levels up to $4.6\,\mathrm{m\,s^{-1}}$. However, it was observed that while a trimmed flight was achieved following the gust excitation, the new trim condition differed from the initial one. After the gust, the elevator input adjusted to a new value, resulting in a different pitch angle, although the altitude was maintained. This suggests that the gust disturbance caused a shift in the trimmed condition. In this new condition, the NMPC prioritized maintaining the flight path, which could not be achieved simultaneously with meeting the orientation tar-

Journal of Computational and Nonlinear Dynamics. December 11, 2024;
Accepted manuscript posted April 11, 2025. 10.1115/1.4068426

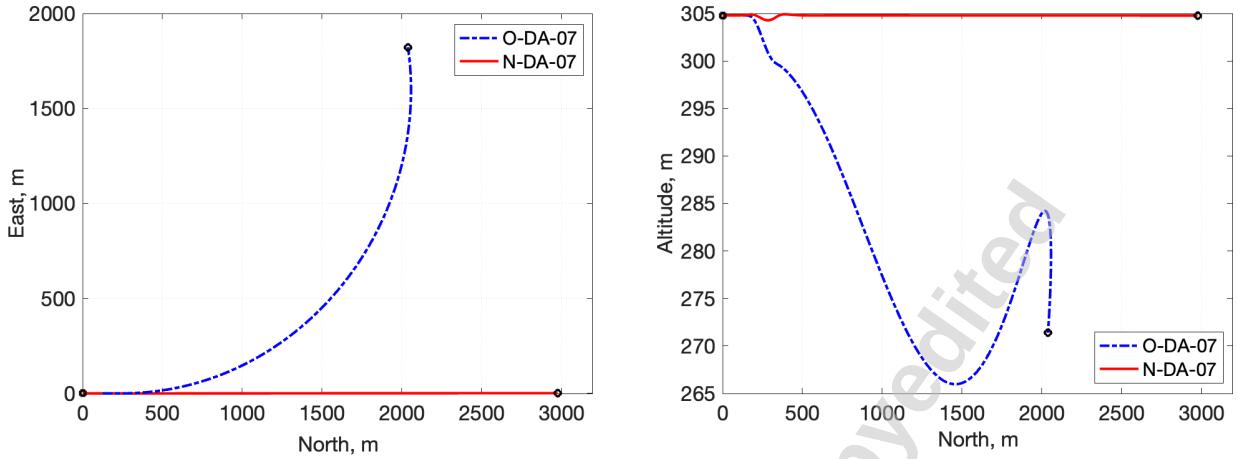

Fig. 27: Aircraft trajectory response during flight with 6.62 m/s maximum magnitude asymmetric discrete gust excitation

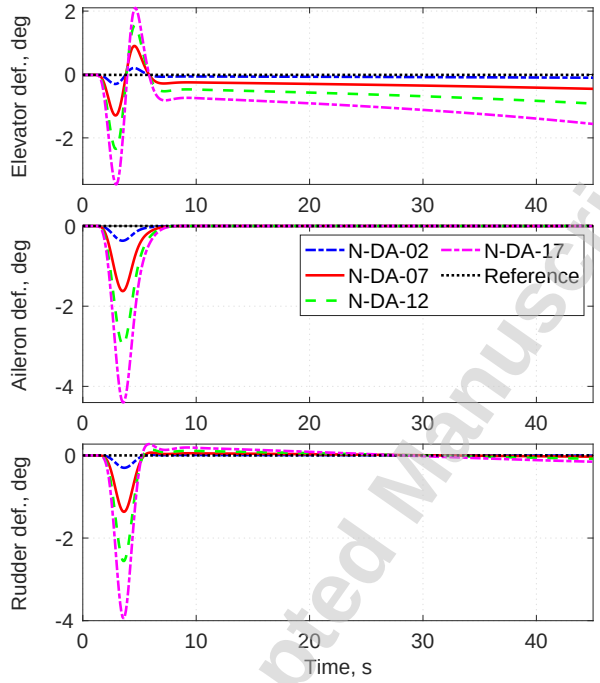

Fig. 28: Control surfaces inputs during flight with asymmetric discrete gust excitation for different maximum magnitudes

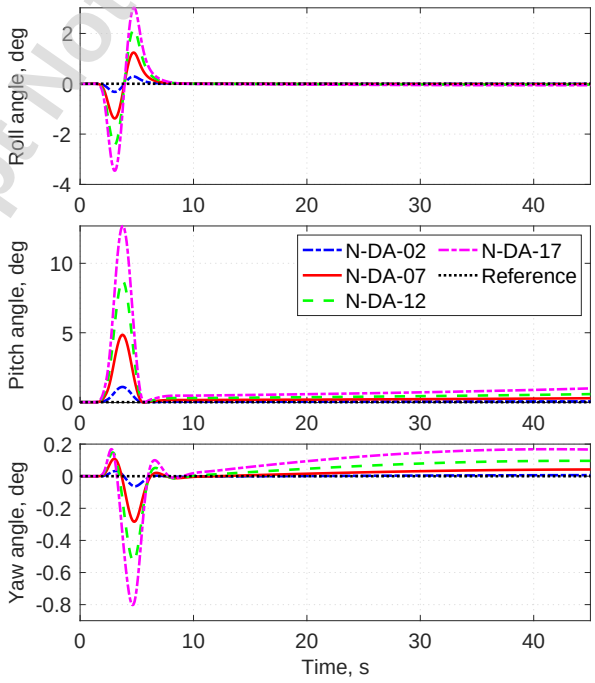

Fig. 29: Euler angle response during flight with asymmetric discrete gust excitation for different maximum magnitudes

gets (Euler angles). For higher turbulence intensities of $5.1\,\mathrm{m\,s^{-1}}$, the NMPC failed to maintain the desired flight path, indicating a limit at which it is no longer effective. The decrease in control effectiveness can be linked to an increased pitch rate. Including this parameter in the controller output vector can expand the range of gust intensities for which the control is still effective for path tracking.

A similar pattern was observed in the case of discrete gusts, where the NMPC successfully maintained the flight

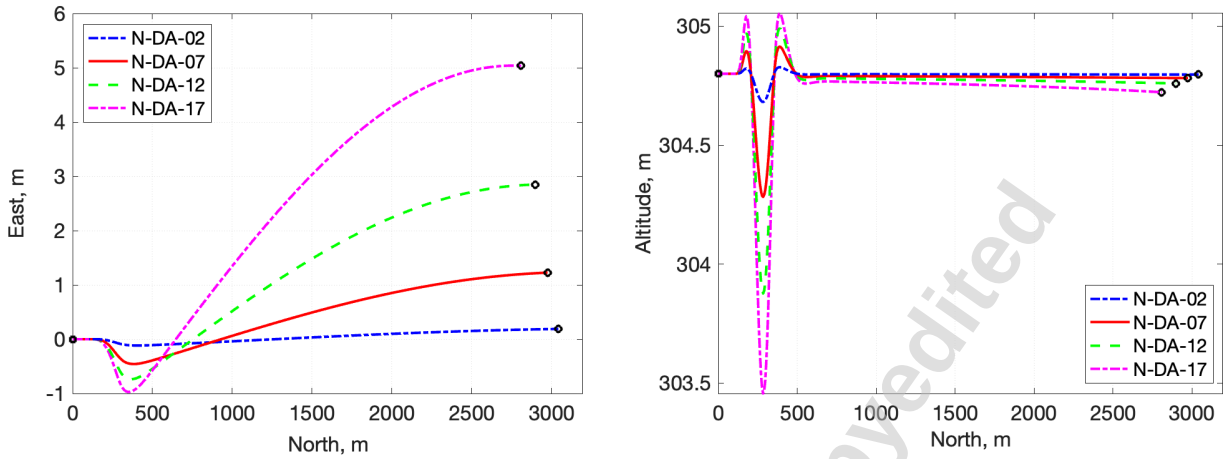

Fig. 30: Aircraft trajectory response during flight with asymmetric discrete gust excitation for different maximum magnitudes

path for both symmetric and asymmetric gusts with deviations in elevator input and pitch angle response. In this scenario, a trimmed flight after the gust disturbance was not achieved. The elevator input exhibited a gradual increase, leading to a corresponding rise in pitch angle magnitude. Similarly, the NMPC prioritized path tracking, achieving good performance at the expense of reduced accuracy in maintaining the desired aircraft orientation. Additionally, an increase in path deviation was observed with higher discrete gust intensities, resulting in larger pitch angles and eastward path deviations. However, in all gust control cases studied, the NMPC results showed significant improvement in path tracking compared to the open-loop response, which exhibited significant altitude drop and severe aircraft turning due east in the cases of asymmetric gust.

The high computational cost of NMPC continues to be a significant challenge for the proposed method. At present, a 60 s flight simulation requires 8 h of computation time, which hinders its use for real-time flight control. One potential solution is using a Neural Network-based NMPC, which can reduce the time required to obtain the optimal NMPC input by employing a neural network approximation of the aircraft model for future predictions instead of relying on the full system model. This approach is currently being explored for future research.

REFERENCES

[1] Tuncer, U. A., 2022, "Urban air mobility industry outlook," *IGLUS Quarterly,* **8**(1), pp. 18–26.

[2] Goyal, R., Reiche, C., Fernando, C., Serrao, J., Kimmel, S., Cohen, A., and Shaheen, S., 2018, Urban air mobility (UAM) market study Tech. Rep. HQ-E-DAA-TN65181, National Aeronautics and Space Administration.

[3] Reiche, C., McGillen, C., Siegel, J., and Brody, F., 2019, "Are we ready to weather urban air mobility UAM?," In 2019 Integrated Communications, Navigation and Surveillance Conference (ICNS), IEEE, pp. 2E21–2E27.

[4] Holden, J., and Goel, N., 2016, Fast-forwarding to a future of on-demand urban air transportation Tech. rep., Uber Technologies Inc., Oct.

[5] Zhou, Y., Zhao, H., and Liu, Y., 2020, "An evaluative review of the VTOL technologies for unmanned and manned aerial vehicles," *Computer Communications,* **149**, pp. 356–369.

[6] Straubinger, A., Rothfeld, R., Shamiyeh, M., Büchter, K.-D., Kaiser, J., and Plötner, K. O., 2020, "An overview of current research and developments in urban air mobility – setting the scene for UAM introduction," *Journal of Air Transport Management,* **87**, p. 101852.

[7] Kim, H. D., Perry, A. T., and Ansell, P. J., 2018, "A review of distributed electric propulsion concepts for air vehicle technology," In 2018 AIAA/IEEE Electric Aircraft Technologies Symposium (EATS), American Institute of Aeronautics and Astronautics.

[8] Braman, G. D., 2018, "Aircraft accidents: Investigating human error," In 2018 Annual Reliability and Maintainability Symposium (RAMS), IEEE.

[9] Zhao, Y., Guo, J., Bai, C., and Zheng, H., 2021, "Reinforcement learning-based collision avoidance guidance algorithm for fixed-wing UAVs," *Com-*

plexity, **2021**(1), p. 8818013.

[10] Zhang, T., Barakos, G. N., Filippone, A., and Furqan, M., 2024, "High-fidelity aero-acoustic evaluations of a heavy-lift eVTOL in hover," *Journal of Sound and Vibration,* **584**, Aug., p. 118453.

[11] Farazi, N. P., and Zou, B., 2024, "Planning electric vertical takeoff and landing aircraft eVTOL-based package delivery with community noise impact considerations," *Transportation Research Part E: Logistics and Transportation Review,* **189**, p. 103661.

[12] Kumar, S. N. T., Duba, P. K., Mannam, N. P. B., Mutnuri, V. S., and Rajalakshmi, P., 2024, "Aeroacoustics and vibration analysis of multirotor eVTOL for sustainable urban air mobility (UAM)," *IEEE Sensors Letters,* **8**(5), May.

[13] Kim, J., Gadsden, S. A., and Wilkerson, S. A., 2019, "A comprehensive survey of control strategies for autonomous quadrotors," *Canadian Journal of Electrical and Computer Engineering,* **43**(1), pp. 3–16.

[14] Hoffmann, G., Huang, H., Waslander, S., and Tomlin, C., 2007, "Quadrotor helicopter flight dynamics and control: Theory and experiment," In AIAA Guidance, Navigation and Control Conference and Exhibit, p. 6461.

[15] Zhang, J., Sun, L., Qu, X., and Wang, L., 2018, "Time-varying linear control for tiltrotor aircraft," *Chinese Journal of Aeronautics,* **31**(4), pp. 632–642.

[16] Bao, X., Kirsch, N., Dodson, A., and Sharma, N., 2019, "Model predictive control of a feedback-linearized hybrid neuroprosthetic system with a barrier penalty," *Journal of Computational and Nonlinear Dynamics,* **14**(10), p. 101009.

[17] Boruah, N., and Roy, B. K., 2020, "A novel event-triggered active model predictive control for synchronization of discrete-time chaotic systems," *Journal of Computational and Nonlinear Dynamics,* **15**(10), p. 101006.

[18] Camacho, E. F., and Bordons, C., 2007, *Model Predictive Control*, 2 ed. Advanced Textbooks in Control and Signal Processing. Springer London.

[19] Kouvaritakis, B., and Cannon, M., 2016, *Model Predictive Control: Classical, Robust and Stochastic* Advanced Textbooks in Control and Signal Processing. Springer Cham.

[20] Qin, S. J., and Badgwell, T. A., 2003, "A survey of industrial model predictive control technology," *Control Engineering Practice,* **11**(7), pp. 733–764.

[21] García, C. E., Prett, D. M., and Morari, M., 1989, "Model predictive control: Theory and practice–a survey," *Automatica,* **25**(3), pp. 335–348.

[22] Morari, M., and Lee, J. H., 1999, "Model predictive control: Past, present and future," *Computers & Chemical Engineering,* **23**(4-5), pp. 667–682.

[23] Mayne, D. Q., Rawlings, J. B., Rao, C. V., and Scokaert, P. O. M., 2000, "Constrained model predictive control: Stability and optimality," *Automatica,* **36**(6), pp. 789–814.

[24] Allgöwer, F., and Zheng, A., eds., 2000, *Nonlinear Model Predictive Control*, Vol. 26 of *Progress in Systems and Control Theory* Birkhäuser Verlag.

[25] Kouvaritakis, B., and Cannon, M., 2001, *Non-Linear Predictive Control: Theory and Practice* The Institution of Engineering and Technology.

[26] Bordons, C., Garcia-Torres, F., and Ridao, M. A., 2020, "Model predictive control fundamentals," In *Model Predictive Control of Microgrids*, Progress in Systems and Control Theory. Springer, pp. 25–44.

[27] He, T., and Su, W., 2023, "Robust control of gust-induced vibration of highly flexible aircraft," *Aerospace Science and Technology,* **143**, p. 108703.

[28] Meradi, D., Benselama, Z. A., and Hedjar, R., 2022, "A predictive sliding mode control for quadrotor's tracking trajectory subject to wind gusts and uncertainties," *International Journal of Electrical and Computer Engineering (IJECE),* **12**(5), pp. 4861–4875.

[29] Nunes, J. S. M., Su, W., and He, T., 2025, "Vibration suppression and trajectory tracking with nonlinear model predictive control for urban air mobility aircraft," *Journal of Dynamic Systems, Measurement, and Control,* **147**(4), p. 041010.

[30] Nunes, J. S. M., Su, W., and He, T., submitted 2024, under revision, "Nonlinear model predictive control for stabilizing tiltrotor urban air mobility aircraft under control effector failures," *Aerospace Science and Technology*.

[31] Su, W., Qu, S., Zhu, G., Swei, S. S.-M., Hashimoto, M., and Zeng, T., 2022, "Modeling and control of a class of urban air mobility tiltrotor aircraft," *Aerospace Science and Technology,* **124**, p. 107561.

[32] Takács, G., and Rohal'-Ilkiv, B., 2012, *Model predictive vibration control: efficient constrained MPC vibration control for lightly damped mechanical structures* Springer Science and Business Media.

[33] Giesseler, H. G., Kopf, M., Varutti, P., Faulwasser, T., and Findeisen, R., 2012, "Model predictive control for gust load alleviation," *IFAC Proceedings Volumes,* **45**(17), pp. 27–32.

[34] Liu, Y., Druyor, C. T., and Wang, L., 2023, "High-fidelity analysis of Lift+Cruise VTOL urban air mobility concept aircraft," In AIAA AVIATION 2023 Forum, p. 3671.

[35] Johnson, W., and Silva, C., 2022, "NASA concept vehicles and the engineering of advanced air mobility aircraft," *The Aeronautical Journal,* **126**(1295), pp. 59–91.

[36] US Department of Defense, 1980, Flying qualities of piloted airplanes Tech. Rep. MIL-F-8785C, US Military, Nov.

[37] Grauer, J. A., Morelli, E. A., and Murri, D. G., 2017, "Flight-test techniques for quantifying pitch rate and angle-of-attack rate dependencies," *Journal of Aircraft,* **54**(6), pp. 2367–2377.

A NONLINEAR MODEL PREDICTIVE CONTROLLER SETTINGS

The table below presents the summary of the NMPC settings for each simulation case presented herein.

- Case ID - *1-23-4*
  - 1: open-loop (O) or NMPC (N) simulations
  - 2: type of gust excitation. S for continuous stochastic gust and D for discrete gust
  - 3: informs of symmetric (S) or asymmetric (A) gust excitation
  - 4: additional information
- Description
- Tiltrotor initial angle - 90° for upward
- t_f - length of simulation in seconds
- dt - simulation time step in seconds
- Input vector - applicable for NMPC. Open-loop uses all system inputs
- p - NMPC prediction horizon
- n - NMPC control horizon
- Output weight ω^y - weights for each y variable before and after control failure
- Output weight ω^u - weights for each u variable before and after control failure
- $\pm u_{lim}$ - upper and lower limits for NMPC inputs
- $\pm \Delta u_{lim}$ - upper and lower limits for NMPC input rate

Table 6: Setting for Gust Excitation Analysis

Case ID	Description	Rotor initial angle, deg	t_f, s	dt, s	Output vector $\mathbf{y}$	Input vector $\mathbf{u}$	p	n	Output weight $\mathbf{!^y}$	Input weight $\mathbf{!^u}$	$\pm\mathbf{u_{lim}}$	$\pm\Delta\mathbf{u_{lim}}$
O-SS-41	Open loop results for symmetric turbulence intensity σ_w of $4.1\,\mathrm{m\,s^{-1}}$	$\{90,90,0,0,0,0\}$	45	0.1	$\{\phi,\theta,\psi,p^G_{B,x},p^G_{B,y},p^G_{B,z}\}$	Eq. 8	-	-	-	-	-	-
O-SA-41	Open loop results for asymmetric turbulence intensity σ_w of $4.1\,\mathrm{m\,s^{-1}}$	$\{90,90,0,0,0,0\}$	45	0.1	$\{\phi,\theta,\psi,p^G_{B,x},p^G_{B,y},p^G_{B,z}\}$	Eq. 8	-	-	-	-	-	-
O-DS-17	Open loop results for symmetric discrete gust with max velocity of $16.8\,\mathrm{m\,s^{-1}}$	$\{90,90,0,0,0,0\}$	45	0.1	$\{\phi,\theta,\psi,p^G_{B,x},p^G_{B,y},p^G_{B,z}\}$	Eq. 8	-	-	-	-	-	-
O-DA-07	Open loop results for asymmetric discrete gust with max. velocity of $6.62\,\mathrm{m\,s^{-1}}$	$\{90,90,0,0,0,0\}$	45	0.1	$\{\phi,\theta,\psi,p^G_{B,x},p^G_{B,y},p^G_{B,z}\}$	Eq. 8	-	-	-	-	-	-
N-SS-41	NMPC results for symmetric turbulence intensity σ_w of $4.1\,\mathrm{m\,s^{-1}}$	$\{90,90,0,0,0,0\}$	45	0.1	$\{\phi,\theta,\psi,p^G_{B,x},p^G_{B,y},p^G_{B,z}\}$	$\Delta\{\delta_e,\delta_a,\delta_r,\dot{\Gamma}_3,\dot{\Gamma}_4\}$	10	1	$\{0.5,0.5,0.5,0.5,0.5,0\}$	$\{0.1,0.1,0.1,0.1,0.1\}$	$\{5,5,5,100,100\}$	$\{5,5,5,100,100\}$
N-SS-46	NMPC results for symmetric turbulence intensity σ_w of $4.6\,\mathrm{m\,s^{-1}}$	$\{90,90,0,0,0,0\}$	45	0.1	$\{\phi,\theta,\psi,p^G_{B,x},p^G_{B,y},p^G_{B,z}\}$	$\Delta\{\delta_e,\delta_a,\delta_r,\dot{\Gamma}_3,\dot{\Gamma}_4\}$	10	1	$\{0.5,0.5,0.5,0.5,0.5,0\}$	$\{0.1,0.1,0.1,0.1,0.1\}$	$\{5,5,5,100,100\}$	$\{5,5,5,100,100\}$
N-SS-51	NMPC results for symmetric turbulence intensity σ_w of $5.1\,\mathrm{m\,s^{-1}}$	$\{90,90,0,0,0,0\}$	45	0.1	$\{\phi,\theta,\psi,p^G_{B,x},p^G_{B,y},p^G_{B,z}\}$	$\Delta\{\delta_e,\delta_a,\delta_r,\dot{\Gamma}_3,\dot{\Gamma}_4\}$	10	1	$\{0.5,0.5,0.5,0.5,0.5,0\}$	$\{0.1,0.1,0.1,0.1,0.1\}$	$\{5,5,5,100,100\}$	$\{5,5,5,100,100\}$
N-SS-56	NMPC results for symmetric turbulence intensity σ_w of $5.6\,\mathrm{m\,s^{-1}}$	$\{90,90,0,0,0,0\}$	45	0.1	$\{\phi,\theta,\psi,p^G_{B,x},p^G_{B,y},p^G_{B,z}\}$	$\Delta\{\delta_e,\delta_a,\delta_r,\dot{\Gamma}_3,\dot{\Gamma}_4\}$	10	1	$\{0.5,0.5,0.5,0.5,0.5,0\}$	$\{0.1,0.1,0.1,0.1,0.1\}$	$\{5,5,5,100,100\}$	$\{5,5,5,100,100\}$
N-SA-41	NMPC results for asymmetric turbulence intensity σ_w of $4.1\,\mathrm{m\,s^{-1}}$	$\{90,90,0,0,0,0\}$	45	0.1	$\{\phi,\theta,\psi,p^G_{B,x},p^G_{B,y},p^G_{B,z}\}$	$\Delta\{\delta_e,\delta_a,\delta_r,\dot{\Gamma}_3,\dot{\Gamma}_4\}$	10	1	$\{0.5,0.5,0.5,0.5,0.5,0\}$	$\{0.1,0.1,0.1,0.1,0.1\}$	$\{5,5,5,100,100\}$	$\{5,5,5,100,100\}$
N-SA-46	NMPC results for asymmetric turbulence intensity σ_w of $4.6\,\mathrm{m\,s^{-1}}$	$\{90,90,0,0,0,0\}$	45	0.1	$\{\phi,\theta,\psi,p^G_{B,x},p^G_{B,y},p^G_{B,z}\}$	$\Delta\{\delta_e,\delta_a,\delta_r,\dot{\Gamma}_3,\dot{\Gamma}_4\}$	10	1	$\{0.5,0.5,0.5,0.5,0.5,0\}$	$\{0.1,0.1,0.1,0.1,0.1\}$	$\{5,5,5,100,100\}$	$\{5,5,5,100,100\}$
N-SA-51	NMPC results for asymmetric turbulence intensity σ_w of $5.1\,\mathrm{m\,s^{-1}}$	$\{90,90,0,0,0,0\}$	45	0.1	$\{\phi,\theta,\psi,p^G_{B,x},p^G_{B,y},p^G_{B,z}\}$	$\Delta\{\delta_e,\delta_a,\delta_r,\dot{\Gamma}_3,\dot{\Gamma}_4\}$	10	1	$\{0.5,0.5,0.5,0.5,0.5,0\}$	$\{0.1,0.1,0.1,0.1,0.1\}$	$\{5,5,5,100,100\}$	$\{5,5,5,100,100\}$
N-DS-02	NMPC results for symmetric discrete gust with max. velocity of $1.52\,\mathrm{m\,s^{-1}}$	$\{90,90,0,0,0,0\}$	45	0.1	$\{\phi,\theta,\psi,p^G_{B,x},p^G_{B,y},p^G_{B,z}\}$	$\Delta\{\delta_e,\delta_a,\delta_r,\dot{\Gamma}_3,\dot{\Gamma}_4\}$	10	1	$\{0.5,0.5,0.5,0.5,0.5,0\}$	$\{0.1,0.1,0.1,0.1,0.1\}$	$\{5,5,5,100,100\}$	$\{5,5,5,100,100\}$
N-DS-07	NMPC results for symmetric discrete gust with max. velocity of $6.62\,\mathrm{m\,s^{-1}}$	$\{90,90,0,0,0,0\}$	45	0.1	$\{\phi,\theta,\psi,p^G_{B,x},p^G_{B,y},p^G_{B,z}\}$	$\Delta\{\delta_e,\delta_a,\delta_r,\dot{\Gamma}_3,\dot{\Gamma}_4\}$	10	1	$\{0.5,0.5,0.5,0.5,0.5,0\}$	$\{0.1,0.1,0.1,0.1,0.1\}$	$\{5,5,5,100,100\}$	$\{5,5,5,100,100\}$
N-DS-12	NMPC results for symmetric discrete gust with max. velocity of $11.73\,\mathrm{m\,s^{-1}}$	$\{90,90,0,0,0,0\}$	45	0.1	$\{\phi,\theta,\psi,p^G_{B,x},p^G_{B,y},p^G_{B,z}\}$	$\Delta\{\delta_e,\delta_a,\delta_r,\dot{\Gamma}_3,\dot{\Gamma}_4\}$	10	1	$\{0.5,0.5,0.5,0.5,0.5,0\}$	$\{0.1,0.1,0.1,0.1,0.1\}$	$\{5,5,5,100,100\}$	$\{5,5,5,100,100\}$
N-DS-17	NMPC results for symmetric discrete gust with max. velocity of $16.8\,\mathrm{m\,s^{-1}}$	$\{90,90,0,0,0,0\}$	45	0.1	$\{\phi,\theta,\psi,p^G_{B,x},p^G_{B,y},p^G_{B,z}\}$	$\Delta\{\delta_e,\delta_a,\delta_r,\dot{\Gamma}_3,\dot{\Gamma}_4\}$	10	1	$\{0.5,0.5,0.5,0.5,0.5,0\}$	$\{0.1,0.1,0.1,0.1,0.1\}$	$\{5,5,5,100,100\}$	$\{5,5,5,100,100\}$
N-DA-02	NMPC results for asymmetric discrete gust with max. velocity of $1.52\,\mathrm{m\,s^{-1}}$	$\{90,90,0,0,0,0\}$	45	0.1	$\{\phi,\theta,\psi,p^G_{B,x},p^G_{B,y},p^G_{B,z}\}$	$\Delta\{\delta_e,\delta_a,\delta_r,\dot{\Gamma}_3,\dot{\Gamma}_4\}$	10	1	$\{0.5,0.5,0.5,0.5,0.5,0\}$	$\{0.1,0.1,0.1,0.1,0.1\}$	$\{5,5,5,100,100\}$	$\{5,5,5,100,100\}$
N-DA-07	NMPC results for asymmetric discrete gust with max. velocity of $6.62\,\mathrm{m\,s^{-1}}$	$\{90,90,0,0,0,0\}$	45	0.1	$\{\phi,\theta,\psi,p^G_{B,x},p^G_{B,y},p^G_{B,z}\}$	$\Delta\{\delta_e,\delta_a,\delta_r,\dot{\Gamma}_3,\dot{\Gamma}_4\}$	10	1	$\{0.5,0.5,0.5,0.5,0.5,0\}$	$\{0.1,0.1,0.1,0.1,0.1\}$	$\{5,5,5,100,100\}$	$\{5,5,5,100,100\}$
N-DA-12	NMPC results for asymmetric discrete gust with max. velocity of $11.73\,\mathrm{m\,s^{-1}}$	$\{90,90,0,0,0,0\}$	45	0.1	$\{\phi,\theta,\psi,p^G_{B,x},p^G_{B,y},p^G_{B,z}\}$	$\Delta\{\delta_e,\delta_a,\delta_r,\dot{\Gamma}_3,\dot{\Gamma}_4\}$	10	1	$\{0.5,0.5,0.5,0.5,0.5,0\}$	$\{0.1,0.1,0.1,0.1,0.1\}$	$\{5,5,5,100,100\}$	$\{5,5,5,100,100\}$
N-DA-17	NMPC results for asymmetric discrete gust with max. velocity of $16.8\,\mathrm{m\,s^{-1}}$	$\{90,90,0,0,0,0\}$	45	0.1	$\{\phi,\theta,\psi,p^G_{B,x},p^G_{B,y},p^G_{B,z}\}$	$\Delta\{\delta_e,\delta_a,\delta_r,\dot{\Gamma}_3,\dot{\Gamma}_4\}$	10	1	$\{0.5,0.5,0.5,0.5,0.5,0\}$	$\{0.1,0.1,0.1,0.1,0.1\}$	$\{5,5,5,100,100\}$	$\{5,5,5,100,100\}$

LIST OF FIGURES